

Recent Developments of the GRP Method*

Joseph FALCOVITZ** and Matania BEN-ARTZI***

A review of about a decade of development of the generalized Riemann problem (GRP) scheme is presented. The method is briefly outlined, followed by various numerical and physical extensions. The range of versatile applications of the GRP method is illustrated through numerous examples.

Key Words : Generalized Riemann Problem, Conservation Laws Scheme, High-Resolution Simulation, Shock Wave Phenomena

1. Introduction

The GRP (generalized Riemann problem) method was introduced in Refs.(5)-(8), following the pioneering work of van Leer⁽³³⁾.

Basically, the GRP is an "analytic high-resolution" (second-order) extension of the classical Godunov⁽¹⁹⁾ scheme, designed to solve numerically systems of conservation or "quasi-conservation" laws. One can also describe the method as a sort of "hybrid" scheme, incorporating the detailed analysis of the characteristic structure at singularities (jumps, edges of rarefaction, imposed boundaries, etc.) into a robust "shock capturing" method, based on conservative differencing.

The fundamental GRP strategy can be summarized as follows (for quasi 1-D problems).

(a) Use piecewise linear distribution of flow variables at a given time level.

(b) Apply the GRP analysis to evaluate fluxes at "singularities". These include, naturally, all jumps at "cell boundaries", but, optionally, also at selected strong shocks, material interfaces and so on.

(c) Use the fluxes in a straightforward time-marching of flow variables, via conservative differencing.

(d) Apply once again the GRP analysis to determine the piecewise linear (i.e., constant slopes in

cells) distribution of flow variables at the new time level.

The above four steps have been used as the underlying basis of a unified approach towards the study of a wide range of fluid dynamical phenomena. It is always expected that the (necessary) additional technicalities (such as monotonicity algorithms or spatial splitting for 2-D problems) are kept at the simplest possible level.

The purpose of this review is to illustrate the broad applicability of the GRP method, subject to its fundamental principles as discussed above. We intend to give an informative and clear description, yet avoid excessive details. For the latter, references to original articles are given.

The analysis of the GRP as presented here follows the original treatment⁽⁵⁾⁻⁽⁸⁾, where characteristic coordinates are used in the resolution of centered waves. We point out that another asymptotic method, based on "similarity coordinates", has been developed and applied by Bourgeade, Le Floch and Raviart^{(10),(11),(26)}.

The plan of this paper is as follows. In Section 2 we discuss the general outline of the GRP methodology and briefly review the underlying analysis. In Section 3 we give some details of the numerical implementation of the method. We begin by presenting a hierarchy of Lagrangian and Eulerian schemes which stem from the GRP philosophy. In particular, we discuss the fundamental L_1, E_1 schemes, which are the simplest second-order extensions to Godunov's scheme. At the other extreme we have L_∞, E_∞ , where the full power of the GRP analysis is invoked. As a

* Received 5th December, 1994.

** Department of Aerospace Engineering, Technion — Israel Institute of Technology, Haifa 32000, Israel

*** Institute of Mathematics, Hebrew University, Jerusalem 91904, Israel

result of the general GRP analysis, we are able to use arbitrary points as grid-points and follow them, achieving an "arbitrary Lagrangian Eulerian" (ALE) version of the GRP scheme, which is also discussed in Section 3. Finally, we discuss the (simple) monotonicity algorithm used in our GRP codes and conclude the section by presenting results for the well-known "Sod shock-tube". In Section 4 we give some physical extensions of the basic fluid-dynamical system and discuss the way they are incorporated in the GRP approach. We concentrate mostly on combustion problems, even though many other applications are possible. In Section 5 we discuss the two-dimensional extension of the GRP method via a suitable "split" scheme. We outline briefly the modifications needed when many materials or moving boundaries are present. Finally, in Section 6 we give a variety of physically interesting numerical examples (in addition to the examples presented in the previous sections as illustrations of the mathematical aspects).

2. General Outline of the GRP Methodology

2.1 Compressible (quasi 1-D) duct flows

Consider the Euler equations that model the time-dependent flow of an inviscid, compressible fluid through a duct of smoothly varying cross-section. We denote by r the spatial coordinate and by $A(r)$ the area of the cross-section at r . The Euler equations can be written in the following form.

$$A \frac{\partial}{\partial t} U + \frac{\partial}{\partial r} [AF(U)] + A \frac{\partial}{\partial r} G(U) = 0, \quad (2.1)$$

$$U = \begin{pmatrix} \rho \\ \rho u \\ \rho E \end{pmatrix}, \quad F(U) = \begin{pmatrix} \rho u \\ \rho u^2 \\ (\rho E + p)u \end{pmatrix}, \quad G(U) = \begin{pmatrix} 0 \\ p \\ 0 \end{pmatrix}.$$

Here ρ, p, u, E are, respectively, density, pressure, velocity and total specific energy, where $E = e + (1/2)u^2$, e being the internal specific energy. In general, the thermodynamic variables p, ρ, e are related by an "equation of state". We shall frequently refer to the most common case, that of an ideal " γ -law" gas, where

$$p = (\gamma - 1)\rho e, \quad \gamma > 1. \quad (2.2)$$

In order to describe the motivation for the analytic problem, let us recall first the approach, originated by Godunov⁽¹⁹⁾, for a conservative ("upwind") difference scheme for Eq. (2.1). Thus, suppose that we use equally spaced grid-points $r_i = i\Delta r$ along the r -axis and the (numerical) solution is sought at equally spaced time levels $t_n = n\Delta t$. By "cell i " we shall refer to the interval extending between the "cell-boundaries" $r_{i\pm 1/2} = (i \pm 1/2)\Delta r$. We label by Q_i^n the average value of a quantity (flow variable) Q over

cell i at time level t_n . Similarly, $Q_{i+1/2}^{n+1/2}$ is the value of Q at the cell boundary $r_{i+1/2}$, averaged over the time interval (t_n, t_{n+1}) . Generally speaking, a "quasi-conservative" difference scheme for Eq. (2.1) is given by

$$U_i^{n+1} - U_i^n = -\frac{\Delta t}{\Delta V_i} \left\{ \left[A(r_{i+1/2})F(U)_{i+1/2}^{n+1/2} - A(r_{i-1/2})F(U)_{i-1/2}^{n+1/2} \right] + A(r_i) \left[G(U)_{i+1/2}^{n+1/2} - G(U)_{i-1/2}^{n+1/2} \right] \right\}, \quad (2.3)$$

where $\Delta V_i = \int_{r_{i-1/2}}^{r_{i+1/2}} A(r) dr$ is the volume of cell i .

In Eq. (2.3) we must still give an appropriate interpretation to the "flux" values $F(U)_{i+1/2}^{n+1/2}$, $G(U)_{i+1/2}^{n+1/2}$. To do this, Godunov proposed to solve (at every cell-boundary $r_{i+1/2}$) the Riemann problem (RP),

$$A \frac{\partial}{\partial t} U + \frac{\partial}{\partial r} [AF(U)] + A \frac{\partial}{\partial r} G(U) = 0, \quad (2.4)$$

$$U(r, 0) = \begin{cases} U_{i+1}^n, & r > r_{i+1/2}, \\ U_i^n, & r < r_{i+1/2}. \end{cases}$$

If the solution thus obtained (for r in the vicinity of $r = r_{i+1/2}$ and $t \geq 0$) is denoted by $U(r, t)$, then the desired flux values are obtained by

$$U_{i+1/2}^{n+1/2} = \lim_{t \rightarrow 0^+} U(r_{i+1/2}, t), \quad F(U)_{i+1/2}^{n+1/2} = F\left(U_{i+1/2}^{n+1/2}\right), \quad (2.5)$$

$$G(U)_{i+1/2}^{n+1/2} = G\left(U_{i+1/2}^{n+1/2}\right).$$

In particular, if $A(r) \equiv 1$ (planar symmetry), the solution to the RP (2.4) is "self-similar" (i.e., depending only on the similarity coordinate r/t) and the classical Godunov scheme is obtained. It is well known⁽²⁹⁾ that the resulting (first-order) scheme is stable and robust, but also that jump discontinuities are poorly resolved by it.

In order to obtain a second-order variant of the Godunov scheme, van Leer⁽³³⁾ proposed the following idea. Assume that all flow variables are linearly distributed in cells (with jumps at cell boundaries). Let $U_i^n(r) = U_i^n + \{(\Delta U)_i^n / \Delta r\}(r - r_i)$ be the linear distribution of U in cell i (at time t_n). In what follows we shall refer to the constant vectors U_i^n , $(1/\Delta r)(\Delta U)_i^n$, respectively, as the average value and slope of U in cell i (at time t_n).

Instead of Eq. (2.4), let us now solve the generalized Riemann problem, namely, the initial value problem given by

$$A \frac{\partial}{\partial t} U + \frac{\partial}{\partial r} [AF(U)] + A \frac{\partial}{\partial r} G(U) = 0, \quad (2.6)$$

$$U(r, 0) = \begin{cases} U_i^n(r), & r < r_{i+\frac{1}{2}}, \\ U_{i+1}^n(r), & r > r_{i+\frac{1}{2}}. \end{cases}$$

Let $U(r, t)$ be the solution to Eq. (2.6) near $(r, t) = (r_{i+\frac{1}{2}}, 0)$. Note that at the singularity the initial value $U(r, 0)$ jumps from $U_i^n + (1/2)(\Delta U)_i^n$ to $U_{i+1}^n - (1/2)(\Delta U)_{i+1}^n$.

The key idea of the GRP method is to solve the system (2.6) "analytically", and then replace Eq. (2.5) by

$$U_{i+\frac{1}{2}}^{n+\frac{1}{2}} = U_{i+\frac{1}{2}}^n + \frac{\Delta t}{2} \cdot \left[\frac{\partial}{\partial t} U \right]_{i+\frac{1}{2}}^n, \quad (2.7)$$

where

$$U_{i+\frac{1}{2}}^n = \lim_{t \rightarrow 0^+} U(r_{i+\frac{1}{2}}, t) \quad (\text{as in Eq. (2.5)}), \quad (2.8)$$

$$\left[\frac{\partial}{\partial t} U \right]_{i+\frac{1}{2}}^n = \lim_{t \rightarrow 0^+} \frac{\partial}{\partial t} U(r_{i+\frac{1}{2}}, t). \quad (2.9)$$

Once $U_{i+\frac{1}{2}}^{n+\frac{1}{2}}$ is evaluated, one proceeds to compute the fluxes as in Eq. (2.5).

It is seen from Eqs. (2.8)–(2.9) that the analytic requirements of the GRP method are actually reduced to an analytic evaluation of the first two terms in the Taylor expansion (in t) of $U(r_{i+\frac{1}{2}}, t)$.

In the following subsection we describe in more detail the procedures leading to the computation of the limits (2.8)–(2.9). We shall make here just the following comments.

1) The evaluation of $U_{i+\frac{1}{2}}^n$ by Eq. (2.8) requires the solution of a Riemann problem of the type used in the classical Godunov scheme, namely, Eq. (2.4) with $A \equiv 1$.

2) In order to obtain a second-order upgrading of Godunov's scheme, it suffices to determine the time derivative (2.9) with an $O(\Delta t)$ error, since then, by Eq. (2.7), the error in the evaluation of flux terms is of order $O(\Delta t^2)$. We shall see (Section 3.1, E_1 scheme) that allowing such an error enables us to develop an extremely simple modification of

Godunov's scheme. As a matter of fact, it is simple enough to be incorporated easily in any existing code using Godunov's scheme. Furthermore, the numerical examples discussed in this article show that, in the majority of cases, it suffices to use the simplified version. We actually recommend that a GRP-Code be equipped with both the simplified (E_1) scheme and the "fully analytic" (E_∞ , in the language of Section 3) scheme, where the use of the latter is restricted to "difficult" grid-points (e.g., large jumps).

2.2 Analytic solution of the GRP

We formulate here the GRP (2.6) in a slightly different form, namely,

$$A \frac{\partial}{\partial t} U + \frac{\partial}{\partial r} [AF(U)] + A \frac{\partial}{\partial r} G(U) = 0, \quad (2.10)$$

$$U(r, 0) = \begin{cases} U_+ + \frac{r}{\Delta r} (\Delta U)_+, & r > 0, \\ U_- + \frac{r}{\Delta r} (\Delta U)_-, & r < 0, \end{cases}$$

In Eq. (2.10), U_\pm and $(\Delta U)_\pm$ are fixed vectors and $\Delta r > 0$ is fixed. Note that U_\pm are the values of $U(r, 0)$ on the two sides of the initial discontinuity at $r=0$, while $(1/\Delta r)(\Delta U)_\pm$ are the respective initial slopes.

Let $U(r, t)$ be the solution to Eq. (2.10) (see Fig. 1). As explained in the preceding subsection, we focus on the exact evaluation of the quantities

$$U_0 = \lim_{t \rightarrow 0^+} U(0, t), \quad (2.11)$$

$$\left[\frac{\partial}{\partial t} U \right]_0 = \lim_{t \rightarrow 0^+} \frac{\partial}{\partial t} U(0, t). \quad (2.12)$$

As a first step, we note that U_0 , as well as the whole "wave structure" of the solution near $(r, t) = (0, 0)$, depends only on U_\pm . More precisely, we have the following.

Theorem 2.1 Let $U_{RP}(r, t)$ be the solution to the planar Riemann problem ("associated" to the GRP (2.10)),

$$\frac{\partial}{\partial t} U_{RP} + \frac{\partial}{\partial r} [F(U_{RP}) + G(U_{RP})] = 0, \quad (2.13)$$

$$U_{RP}(r, 0) = U_+ \text{ for } r > 0, \\ U_{RP}(r, 0) = U_- \text{ for } r < 0.$$

Then:

(a) The wave patterns of U and U_{RP} near the singularity $(0, 0)$ are identical.

(b) Along any fixed direction $\theta = r/t = \text{const.}$ we have,

$$\lim_{t \rightarrow 0^+} U(\theta t, t) = U_{RP}(\theta t, t) = U_{RP}(\theta, 1), \quad (2.14)$$

and, in particular,

$$U_0 = U_{RP}(0, 1). \quad (2.15)$$

Remark 2.2

(a) The meaning of the first conclusion of the theorem is that the solutions U and U_{RP} display the same waves emanating from the origin (shocks, rarefactions, contact discontinuities), and they propagate

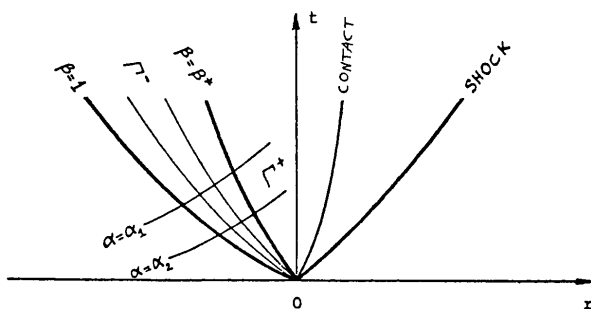


Fig. 1 Structure of solution to GRP in Eulerian coordinates

in the same directions, with the same initial speeds. Both solutions are smooth in the zones (in the upper half (r, t) -plane) between waves, and also within rarefaction fans (between tail and head characteristics).

(b) As is well known, the solution U_{RP} is “self-similar”, i.e., along every fixed direction $-\infty < \theta < \infty$ and for all $t > 0$, $U_{RP}(\theta t, t) = U_{RP}(\theta, 1)$. On the other hand the waves represented by $U(r, t)$ are in general curvilinear (see Fig. 1). However, the asymptotic formula (2.14) means that the two solutions coincide “at the singularity” in every direction. This fact can be viewed as a reflection of the “finite propagation speed” property of the equations. It implies that the resolved wave structure is not immediately affected by either the varying cross-section or the nonconstant initial data.

For a further discussion of Theorem 2.1 or its proof we refer the reader to Refs. (7), (10), (27) and references therein.

We are left with the task of determining $[(\partial/\partial t)U]_0$ (see Eq. (2.12)). The main building block in our solution is the following Lagrangian analysis.

Define a Lagrangian “mass” coordinate by,

$$d\xi = A(r)\rho(r, 0)dr, \quad \xi(0) = 0. \quad (2.16)$$

In terms of (ξ, t) , the GRP (2.10) takes the form

$$\begin{aligned} \frac{\partial}{\partial t} V + \frac{\partial}{\partial \xi} [A\Phi(V)] + A \frac{\partial}{\partial \xi} \Psi(V) &= 0, \\ V &= \begin{pmatrix} \tau \\ u \\ E \end{pmatrix}, \quad \Phi(V) = \begin{pmatrix} -u \\ 0 \\ pu \end{pmatrix}, \\ \Psi(V) &= \begin{pmatrix} 0 \\ p \\ 0 \end{pmatrix}, \quad \tau = \frac{1}{\rho}, \\ V(\xi, 0) &= \begin{cases} V_+ - \frac{\xi}{\Delta \xi} (\Delta V)_+, & \xi > 0, \\ V_- - \frac{\xi}{\Delta \xi} (\Delta V)_-, & \xi < 0. \end{cases} \end{aligned} \quad (2.17)$$

Observe that in $V(\xi, 0)$ we assume linearity in ξ . This is justified since, as follows from the discussion below, the solution (2.12) depends in fact only on the limiting values of the derivatives $(\partial/\partial r)U(r, 0)$ as $r \rightarrow 0 \pm$. Thus, we shall use the notation $\{(\partial/\partial r)Q\}_\pm$ for the initial slopes of any variable Q on either side of the discontinuity and set

$$\left(\frac{\partial Q}{\partial \xi} \right)_\pm = A(0)^{-1} \rho_\pm^{-1} \left(\frac{\partial Q}{\partial r} \right)_\pm. \quad (2.18)$$

In analogy with Fig. 1, we assume that the situation is as shown in Fig. 2, namely, a shock wave propagates to the right and a centered rarefaction wave travels to the left.

These waves are separated by a contact discontinuity ($\xi = 0$), and bound regions of smooth flow (which is uniform only in the case that $A(r) = \text{const.}$

β = normalized slope of C_- at the origin,
 $\beta = 1$ at the head characteristic.
 α = value of ξ at point of intersection
of C_+ with the curve $\beta = 1$.

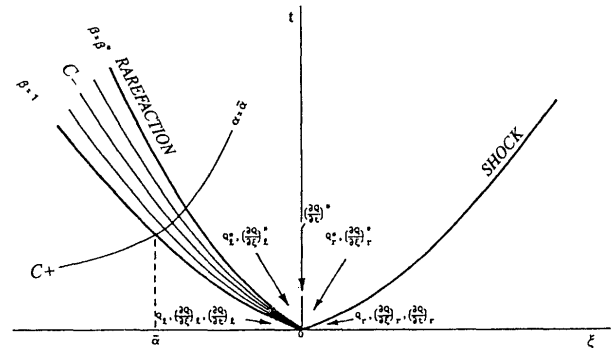


Fig. 2 Structure of solution to GRP in Lagrangian coordinates

and $(\partial V/\partial \xi)_+ = (\partial V/\partial \xi)_- = 0$). Let $V(\xi, t)$ be the solution to Eq. (2.17) (with $(\partial V/\partial \xi)_\pm = (1/\Delta \xi)(\Delta V)_\pm$). We set $V^* = \lim_{t \rightarrow 0^+} V(0, t)$. Note that V^* is obtained as the solution along the contact discontinuity for the planar Riemann problem (2.13). In analogy with Eq. (2.12), we need to compute

$$\left(\frac{\partial V}{\partial t} \right)^* = \lim_{t \rightarrow 0^+} \frac{\partial}{\partial t} V(0, t). \quad (2.19)$$

Note that while u^*, p^* are continuous across the contact discontinuity $\xi = 0$, the density ρ experiences a jump there. We shall use the obvious notation ρ_\pm^* for its values on either side. The main step in the evaluation of Eq. (2.19) is contained in the following theorem, where we follow an idea of van Leer⁽³³⁾. For a detailed proof, see Ref. (5). Here we shall only outline the proof for a γ -law gas (see Eq. (2.2)).

Theorem 2.3 The derivatives $(\partial p/\partial t)^*, (\partial u/\partial t)^*$ are determined by a pair of linear equations,

$$\begin{aligned} a_+ \left(\frac{\partial u}{\partial t} \right)^* + b_+ \left(\frac{\partial p}{\partial t} \right)^* &= d_+, \\ a_- \left(\frac{\partial u}{\partial t} \right)^* + b_- \left(\frac{\partial p}{\partial t} \right)^* &= d_-, \end{aligned} \quad (2.20)$$

where a_+, b_+, d_+ (resp. a_-, b_-, d_-) can be determined explicitly from $V^*, V_+, (\partial V/\partial \xi)_+$ (resp. $V^*, V_-, (\partial V/\partial \xi)_-$).

Sketch of proof (γ -law gas) : We assume the wave configuration of Fig. 2. Along the shock trajectory, for $t > 0$, let u_r, p_r, ρ_r be the pre-shock quantities, u, p the post-shock ones. It follows from the Rankine-Hugoniot jump conditions⁽¹³⁾ that

$$\begin{aligned} u - u_r &= (p - p_r) \left[\frac{1 - \mu^2}{\rho_r (p + \mu^2 p_r)} \right]^{\frac{1}{2}}, \\ \mu^2 &= \frac{\gamma - 1}{\gamma + 1}. \end{aligned} \quad (2.21)$$

Differentiate this identity along the shock trajectory and let the point under consideration tend to the

singularity (i.e., $(u, p) \rightarrow (u^*, p^*)$, $(u_r, p_r, \rho_r) \rightarrow (u_+, p_+, \rho_+)$). Note that, using Eq. (2.17), the t -derivatives ahead of the shock (i.e., of u_r, p_r, ρ_r) can be replaced by ξ -derivatives, which tend to the initial values $(\partial Q/\partial \xi)_+$. Also, behind the shock the ξ -derivatives of u, p can be replaced by linear combinations of t -derivatives of these values, tending to $(\partial u/\partial t)^*$, $(\partial p/\partial t)^*$.

Carrying out all those differentiations and limiting procedures we obtain the following explicit expressions (γ -law gas).

$$\begin{aligned} a_+ &= -2 + \frac{1}{2} \frac{p^* - p_+}{p^* + \mu^2 p_+}, \\ b_+ &= -\frac{u^* - u_+}{2(p^* + \mu^2 p_+)} + A(0)W_+^{-1} \\ &\quad + A(0)^{-1}W_+(\rho_+^* c_+^*)^{-2}, \\ d_+ &= L_u \left(\frac{\partial u}{\partial \xi} \right)_+ + L_p \left(\frac{\partial p}{\partial \xi} \right)_+ \\ &\quad + L_\rho \left(\frac{\partial \rho}{\partial \xi} \right)_+ + \frac{A'(0)}{A(0)} L_g, \end{aligned} \quad (2.22)$$

where $W_+ = A(0)\{(p^* - p_+)/(\rho_+^* - \rho_+)\}$ is the “Lagrangian” shock speed and,

$$\begin{aligned} L_u &= \frac{A(0)}{2} (u_+ - u^*) \left(\rho_+ + \mu^2 \frac{\rho_+^2 c_+^2}{p^* + \mu^2 p_+} \right) \\ &\quad - A(0)^2 W_+^{-1} \rho_+^2 c_+^2 - W_+, \\ L_p &= 2A(0) + \frac{\mu^2}{2} A(0) \frac{p^* - p_+}{p^* + \mu^2 p_+}, \\ L_\rho &= \frac{A(0)}{2} \frac{p^* - p_+}{\rho_+}, \\ L_g &= -W_+ A(0)^{-1} u^* (\rho_+^*)^{-1} - u_+ \rho_+^{-1} (u^* - u_+) \\ &\quad \times \left[\rho_+^2 c_+^2 \left(\frac{1}{p^* - p_+} + \frac{\mu^2}{2} \cdot \frac{1}{p^* + \mu^2 p_+} \right) + \frac{\rho_+}{2} \right]. \end{aligned}$$

(here and below c =speed of sound).

We now turn to the more delicate problem of determining the coefficients a_- , b_- , d_- in Eq. (2.20), assuming the wave configuration of Fig. 2. Here, the general idea is to replace the differentiation of “jump conditions” by a “rotation procedure”, which translates the left-side spatial (initial) derivatives $(\partial Q/\partial \xi)_-$ into the desired time derivatives $(\partial V/\partial t)^*$. Such a procedure constitutes the heart of the GRP method and is based on a careful study of the “propagation of singularities” across a centered rarefaction wave. We remark that the strategy of van Leer⁽³³⁾ at this point was to replace the centered rarefaction wave by a “rarefaction shock”, leading to jump equations analogous to Eq. (2.21) and differentiating them. Such a procedure leads to an “ E_2 -scheme” (see Section 3.1 on “classification of GRP schemes” below and the Appendix in Ref. (5)).

To deal with the centered rarefaction wave we refer to the configuration of Fig. 2 and introduce characteristic coordinates as follows.

β =Normalized slope $(\rho c/\rho_- c_-)$ of Γ^- at the origin, where $\beta=1$ at the head characteristic.

α =Value of ξ at point of intersection of Γ^+ with the curve $\beta=1$.

Every flow variable Q is now represented (throughout the rarefaction zone) by a smooth function $Q(\alpha, \beta)$, up to the singularity $\alpha=0$. Observe that (in analogy with the case of polar coordinates at the origin) the singularity at $\alpha=0$ consists of a full interval of β , corresponding to slopes of all Γ^- characteristic curves spanning the rarefaction. The directional derivative $(\partial Q/\partial \alpha)(0, \beta)$ (which, of course, vanishes for the planar Riemann problem) measures the local variation of Q at the singularity in the direction of the Γ^- characteristic of (normalized) slope β .

The following lemma is essential in the above-mentioned “rotation procedure” of directional derivatives. We formulate it here for the γ -law gas. See Ref. (7) for a general equation of state and a complete proof.

Lemma 2.4 Let $a(\beta) = (\partial u/\partial \alpha)(0, \beta)$, $\beta^* \leq \beta \leq 1$, where $\beta^* = \rho_-^* c_-^* / \rho_- c_-$ is the (normalized) slope of the tail Γ^- -characteristic (Fig. 2). Then $a(\beta)$ is given by

$$\begin{aligned} a(\beta) &= a(1) + \frac{2}{\rho_- c_- (3\gamma - 1)} \left[c_- \left(\frac{\partial(\rho c)}{\partial \xi} \right)_- \right. \\ &\quad \left. - \frac{\gamma + 1}{2} \left(\frac{\partial \rho}{\partial \xi} \right)_- \right] (\beta^{\frac{3\gamma-1}{2(\gamma+1)}} - 1) \\ &\quad + \frac{A'(0)}{A(0)^2} \left[\frac{4c_-}{(3\gamma - 5)\rho_-} (\beta^{\frac{3\gamma-5}{2(\gamma+1)}} - 1) \right. \\ &\quad \left. - \frac{(\gamma - 1)u_- + 2c_-}{(\gamma - 3)\rho_-} (\beta^{\frac{\gamma-3}{2(\gamma+1)}} - 1) \right], \\ a(1) &= \left(\frac{\partial u}{\partial \xi} \right)_- + \rho_-^{-1} c_-^{-1} \left(\frac{\partial p}{\partial \xi} \right)_-. \end{aligned} \quad (2.23)$$

(Eq. (2.23) must be modified for $\gamma=5/3, 3$).

Note that the expression (2.23) simplifies considerably at a “flat” point, where $A'(0)=0$.

With $a(\beta)$ as given by the lemma, we can continue our outline of the proof of Theorem 2.3. We claim that, given the configuration of Fig. 2, the second equation of (2.20) is satisfied with,

$$\begin{aligned} a_- &= 1, \\ b_- &= (\rho_-^* c_-^*)^{-1}, \\ d_- &= -A(0)(\rho_- \rho_-^* c_- c_-^*)^{1/2} a(\beta^*) - \frac{A'(0)}{A(0)} u^* c_-^*. \end{aligned} \quad (2.24)$$

Again, we refer the reader to Ref. (7) for a detailed proof, and give here a sketch as follows.

Write the characteristic equation along the tail characteristic Γ^- at $(0, \beta^*)$ in the form

$$\begin{aligned} \frac{\partial p}{\partial \alpha}(0, \beta^*) - \rho_-^* c_-^* \frac{\partial u}{\partial \alpha}(0, \beta^*) \\ + \frac{A'(0)}{A(0)} \rho_-^* u^* (c_-^*)^2 \frac{\partial t}{\partial \alpha}(0, \beta^*) = 0. \end{aligned} \quad (2.25)$$

It can be shown that,

$$\begin{aligned}\frac{\partial t}{\partial \alpha}(0, \beta^*) &= -(\rho_{-c} A(0))^{-1} (\beta^*)^{-\frac{1}{2}}, \\ \frac{\partial \xi}{\partial \alpha}(0, \beta^*) &= (\beta^*)^{1/2}.\end{aligned}\quad (2.26)$$

Since $a(\beta^*) = (\partial u / \partial \alpha)(0, \beta^*)$ is known, $(\partial p / \partial \alpha)(0, \beta^*)$ can be determined from Eq. (2.25). From the chain rule we obtain

$$\frac{\partial p}{\partial \alpha}(0, \beta^*) = \left(\frac{\partial p}{\partial t} \right)^* \frac{\partial t}{\partial \alpha}(0, \beta^*) + \left(\frac{\partial p}{\partial \xi} \right)^* \frac{\partial \xi}{\partial \alpha}(0, \beta^*). \quad (2.27)$$

From Eq. (2.17) we obtain $(\partial p / \partial \xi)^* = -A(0)^{-1} \times (\partial u / \partial t)^*$, and inserting this in (2.27) yields a linear relation between $(\partial u / \partial t)^*$, $(\partial p / \partial t)^*$ (with a known right-hand side), which is exactly the second equation of (2.20), and the coefficients (2.24) are obtained from Eqs. (2.25)–(2.26).

This concludes the description of the proof of Theorem 2.3. Q. E. D.

Now, we return to Eulerian analysis.

We need to compute $[(\partial / \partial t)U]_0$ as in Eq. (2.12). Assume the configuration of Fig. 1. In particular, we assume that the line $r=0$ (t -axis) is non sonic, i.e., that it is not contained in a rarefaction fan. By means of the transformation (2.16) we switch locally to Lagrangian coordinates, adjusting the initial slopes as in Eq. (2.18). In this new system the line $r=0$ is represented by a curve $\xi = \xi(t)$ satisfying

$$\frac{d\xi}{dt} = -A(0)\rho(\xi, t)u(\xi, t), \quad \xi(0) = 0. \quad (2.28)$$

Indeed, this follows easily by differentiating the identity $r(\xi(t), t) = 0$.

Applying the chain rule and Eq. (2.28) we obtain the following formula for the time derivative $(\partial Q / \partial t)_0$ of any flow variable Q ($Q = \rho, p, u$).

$$\left(\frac{\partial Q}{\partial t} \right)_0 = \left(\frac{\partial Q}{\partial t} \right)^* - A(0)\rho_0 u_0 \left(\frac{\partial Q}{\partial \xi} \right)^* \quad (2.29)$$

($U_0 = U^*$ in the configuration of Fig. 1).

In Eq. (2.29) one must note the following.

(a) While $(\partial p / \partial t)^*$, $(\partial u / \partial t)^*$ are well defined, we have for the density,

$$\left(\frac{\partial \rho}{\partial t} \right)^*_{\pm} = (c_{\pm}^*)^{-2} \left(\frac{\partial p}{\partial t} \right)^*.$$

Obviously, the sign is determined by the side on which $r=0$ falls, relative to the contact discontinuity.

(b) The derivatives $(\partial p / \partial \xi)^*$, $(\partial u / \partial \xi)^*$, i.e., the Lagrangian derivatives at the contact discontinuity, are determined from $(\partial u / \partial t)^*$, $(\partial p / \partial t)^*$ via Eq. (2.17). Note that $(\partial u / \partial \xi)^*$ is discontinuous.

(c) The derivatives $(\partial \rho / \partial \xi)^*$ cannot be determined directly from Eq. (2.17). See Ref. (5) for the details of this derivation.

(d) In the case that the line $r=0$ lies either to the left of the rarefaction wave or to the right of the shock wave (Fig. 1), Eq. (2.29) can be replaced simply by (2.10), using the appropriate initial slopes.

(e) The sonic case. This is the case where the centered rarefaction wave contains the line $r=0$. Thus, at the singularity the line $r=0$ is tangent to a Γ^- -characteristic having slope β_0 . Let $(\alpha(t), \beta(t))$ be the trajectory $r=0$ in the (α, β) plane, with $(\alpha(0), \beta(0)) = (0, \beta_0)$. Since the limiting values at the singularity are those obtained for the planar Riemann problem, it follows that for a γ -law gas

$$\beta_0 = \left[\frac{\gamma-1}{\gamma+1} \left(\frac{u_-}{c_-} + \frac{2}{\gamma-1} \right) \right]^{\frac{\gamma+1}{\gamma-1}}. \quad (2.30)$$

(In the planar case the Γ^- -characteristic of slope β_0 is a straight line which coincides with $r=0$).

In the domain covered by the rarefaction fan all flow variables are represented as functions of (α, β) and Eq. (2.29) is now replaced by

$$\left(\frac{\partial Q}{\partial t} \right)_0 = \frac{\partial Q}{\partial \alpha}(0, \beta_0) \cdot \alpha'(0) + \frac{\partial Q}{\partial \beta}(0, \beta_0) \cdot \beta'(0), \quad (2.31)$$

where one can show that

$$\begin{aligned}\alpha'(0) &= -A(0)\rho_{-c}\beta_0^{1/2}, \\ \beta'(0) &= \frac{1}{2}\beta_0^{1/2}A(0) \left[\frac{\partial}{\partial \alpha}(\rho c)(0, \beta_0) - \frac{\partial}{\partial \alpha}(\rho u)(0, \beta_0) \right].\end{aligned}\quad (2.32)$$

We again refer the reader to Ref. (5) for a detailed discussion and derivation of Eqs. (2.30)–(2.32). Note that in Eq. (2.31) the derivatives $(\partial Q / \partial \beta)(0, \beta_0)$ are evaluated by the solution U_{RP} to the planar Riemann problem (Theorem 2.1 above) while $(\partial Q / \partial \alpha)(0, \beta_0)$ are obtained from the treatment of the centered rarefaction wave (Lemma 2.3).

3. Numerical Implementation

3.1 Classification of GRP schemes: $L_1, L_\infty; E_1, E_\infty$

In the previous section we described the GRP scheme and how it leads to an analytic study of the equations in a neighborhood of a singularity.

The full numerical procedure (for the Eulerian equations (2.1)) may now be summarized as follows.

(a) Start with piecewise linear distributions of flow variables in computational cells, at time level $t_n = n\Delta t$.

(b) Use the GRP analysis to evaluate the derivatives $[(\partial / \partial t)U]_{i+\frac{1}{2}}^{n+\frac{1}{2}}$.

(c) Compute the new cell averages U_i^{n+1} by Eqs. (2.3), (2.7)–(2.9).

(d) Compute new slopes in cells by,

$$\begin{aligned}(\Delta U)_i^{n+1} &= U_{i+\frac{1}{2}}^{n+1} - U_{i-\frac{1}{2}}^{n+1}, \\ \text{where, in analogy with (2.7),} \\ U_{i+\frac{1}{2}}^{n+1} &= U_{i+\frac{1}{2}}^n + \Delta t \cdot \left[\frac{\partial}{\partial t} U \right]_{i+\frac{1}{2}}^n.\end{aligned}\quad (3.1)$$

(e) Modify $(\Delta U)_i^{n+1}$ by a monotonicity algorithm (see Section 3.4 below).

As was clear from the discussion in the preceding section, the above steps could be modified so as to produce a Lagrangian scheme (where grid-points automatically follow particle trajectories). In fact, Eq. (2.29) expresses the Eulerian time derivatives in terms of Lagrangian derivatives, which must be calculated first.

Step (b) above requires the application of the full GRP analysis, so that no error is made in the evaluation of the time derivatives at singularities (given the initial slopes). Therefore we label this scheme as an E_∞ -GRP scheme (and the corresponding Lagrangian version as L_∞).

However, as is seen from Eq. (2.7), if one is only interested in second-order accuracy of the scheme then it suffices to determine $[(\partial/\partial t)U]_{i+\frac{1}{2}}^{n+1}$ up to an $O(\Delta t)$ error (since the fluxes are evaluated to within an $O(\Delta t^2)$ error).

This observation motivates the following claim, which is formulated in the Lagrangian context of the preceding section.

Lemma 3.1 Set in Eqs. (2.20)

$$\begin{aligned} a_\pm &= \mp 1, \quad b_\pm = \rho_\pm^{-1} c_\pm^{-1}, \\ d_\pm &= -A(0) \left(\rho_\pm c_\pm \left(\frac{\partial u}{\partial \xi} \right)_\pm \mp \left(\frac{\partial p}{\partial \xi} \right)_\pm \right) - \frac{A'(0)}{A(0)} u_\pm c_\pm. \end{aligned} \quad (3.2)$$

Then, in regions of smooth flow, $(\partial u/\partial t)^*$, $(\partial p/\partial t)^*$ are obtained from (2.20) to within an $O(\Delta t)$ error.

Proof We give the proof for the “+” sign. In a region of smooth flow we may assume that the right wave is, within an $O(\Delta t)$ error, an “acoustic” wave, namely, a single characteristic curve of slope $d\xi/dt = A\rho c$. Across this curve all variables (hence also their tangential derivatives) are continuous. We may therefore evaluate the directional derivative of p along the curve by using the values either ahead of or behind the wave, obtaining

$$\begin{aligned} A(0) \rho_+ c_+ \left(\frac{\partial p}{\partial \xi} \right)^* + \left(\frac{\partial p}{\partial t} \right)^* \\ = A(0) \rho_+ c_+ \left(\frac{\partial p}{\partial \xi} \right)_+ + \left(\frac{\partial p}{\partial t} \right)_+, \end{aligned} \quad (3.3)$$

where $(\partial p/\partial \xi)^*$ is evaluated just behind the wave while $(\partial p/\partial t)_+$ is evaluated ahead of it. From Eq. (2.17) we obtain

$$\begin{aligned} \left(\frac{\partial p}{\partial \xi} \right)^* &= -A(0)^{-1} \left(\frac{\partial u}{\partial t} \right)^*, \\ \left(\frac{\partial p}{\partial t} \right)_+ &= c_+^2 \left(\frac{\partial \rho}{\partial t} \right)_+ = -\rho_+^2 c_+^2 \left[\frac{\partial}{\partial \xi} A u \right]_+, \end{aligned}$$

where we have used the fact that the entropy is constant along a streamline $\xi = \text{const}$. Noting Eq. (2.16), we have

$$\left[\frac{\partial}{\partial \xi} A u \right]_+ = \frac{u_+ A'(0)}{\rho_+ A(0)} + A(0) \left(\frac{\partial u}{\partial \xi} \right)_+.$$

Inserting all these relations in Eq. (3.3) yields Eq.

(3.2).

Q. E. D.

We may rephrase the above discussion by saying that, a second-order scheme is still obtained if all waves are viewed as “acoustic” waves.

Note, however, that the value of $U_{i+\frac{1}{2}}^{n+1}$ (see Eq. (3.1)), which is also needed in Eq. (2.29) (where it is denoted as U_0), is obtained as a result of a solution to the associated Riemann problem, as given in Eq. (2.15). In fact, since the underlying assumption for the use of the L_1, E_1 schemes is that all waves involved are “weak”, one could use (within the same order of accuracy) a simplified (i.e., approximate) solution to the associated Riemann problem.

As already noted above, the original van Leer scheme⁽³³⁾ is classified in the present hierarchy as an E_2 -scheme (see Appendix in Ref. (5)).

To deal with the Eulerian case, we note that if all waves are “acoustic” (i.e., of “zero strength”), then there is no “sonic case” and the applicable formula for time derivatives is now always Eq. (2.29). We can summarize all these as follows.

L_1, E_1 -Schemes

(i) Use the coefficients a_\pm, b_\pm, d_\pm as given by Eq. (3.2) in Eq. (2.20) and evaluate $(\partial u/\partial t)^*, (\partial p/\partial t)^*$.

(ii) Use Eq. (2.29) in order to evaluate time derivatives $(\partial Q/\partial t)_0$ in the Eulerian frame.

(iii) Repeat the procedure given by steps (c)-(e) in the beginning of this section.

Thus, we obtain either a Lagrangian or an Eulerian scheme, which we label, respectively, as L_1 and E_1 .

It is important to note that there is virtually no additional computational effort involved in upgrading Godunov’s scheme by the above analysis, and that it can be implemented in any existing code.

Observe also that in the L_1, E_1 analysis, the coefficients a_\pm, b_\pm, d_\pm depend only on the initial data $V_\pm, (\partial V/\partial \xi)_\pm$, and not even on V^* . In particular, the detailed GRP analysis of the preceding section is not needed here. Most examples presented in the following sections have been computed in terms of the E_1 scheme.

3.2 ALE analysis

The so-called “arbitrary Lagrangian Eulerian” (ALE) extension is designed to avoid mesh tangling in flows involving large deformations. Our motivation in using an arbitrary mesh comes also from the following consideration. It is desirable to follow (=“track”) various singularities in the flow (shocks, material interfaces, edges of rarefaction waves, etc.) and to use them as grid-points.

The moving grid extension to GRP is formulated as follows.

Consider the Euler duct flow equations (2.1)

in a smoothly moving zone $D_t = \{r | a(t) \leq r \leq b(t)\}$. Assuming that the flow in D_t is smooth so that all flow variables can be differentiated, we obtain the following integral relation.

$$\begin{aligned} -\frac{d}{dt} \int_{D_t} UA(r) dr &= \int_{D_t} \frac{\partial U}{\partial t} A(r) dr \\ &+ b'(t)A(b(t))U(b(t), t) \\ &- a'(t)A(a(t))U(a(t), t). \end{aligned} \quad (3.4)$$

Using the flow equations (2.1), Eq. (3.4) can be rewritten as

$$\begin{aligned} -\frac{d}{dt} \int_{D_t} UA(r) dr &= [(\Lambda U - F(U))A]_{a(t);t}^{b(t);t} \\ &- \int_{D_t} A(r) \frac{\partial}{\partial r} G(U) dr, \end{aligned} \quad (3.5)$$

where $\Lambda(a(t), t) = a'(t)$, $\Lambda(b(t), t) = b'(t)$.

In the present ALE implementation, the interval D_t represents a grid cell moving in an arbitrary fashion with respect to the underlying Eulerian mesh. Its endpoints, denoted now by $r_{i \pm \frac{1}{2}}(t)$, correspond, respectively, to $a(t)$, $b(t)$ in (3.5). Furthermore, we set $r_{i \pm \frac{1}{2}}^n = r_{i \pm \frac{1}{2}}(n\Delta t)$ to be the endpoint values at the n -th time level t_n . For a given flow variable Q , we define Q_i^n and $Q_{i \pm \frac{1}{2}}^{n+\frac{1}{2}}$, respectively, as the average value in cell i at t_n , and the time average value at $r_{i \pm \frac{1}{2}}$ (between t_n and t_{n+1}). In analogy with the difference equation (2.3), Eq. (3.5) is now discretized as

$$\begin{aligned} U_i^{n+1} &= \frac{(\Delta V)_i^n}{(\Delta V)_i^{n+1}} U_i^n \\ &+ \frac{\Delta t}{(\Delta V)_i^{n+1}} [(\Lambda U - F(U))A]_{i+\frac{1}{2}}^{n+\frac{1}{2}} \\ &- [(\Lambda U - F(U))A]_{i-\frac{1}{2}}^{n+\frac{1}{2}} \\ &- \frac{1}{2} [G(U)_{i+\frac{1}{2}}^{n+\frac{1}{2}} - G(U)_{i-\frac{1}{2}}^{n+\frac{1}{2}}] \cdot (A_{i+\frac{1}{2}}^{n+\frac{1}{2}} + A_{i-\frac{1}{2}}^{n+\frac{1}{2}}), \end{aligned} \quad (3.6)$$

where $A_{i \pm \frac{1}{2}}^{n+\frac{1}{2}} = A(r_{i \pm \frac{1}{2}}^{n+\frac{1}{2}})$ and the cell volume $(\Delta V)_i^n = \int_{r_{i-\frac{1}{2}}^n}^{r_{i+\frac{1}{2}}^n} A(r) dr$.

In order to obtain second-order accuracy for the scheme (3.6) we assume again that the values U^n are linearly distributed in cells. The boundary values $U_{i \pm \frac{1}{2}}^{n+\frac{1}{2}}$ are then determined by the GRP analytic method as described above. Note that since cell-boundaries are moving relative to the Eulerian grid, the full GRP method is needed in order to determine the time evolution of flow quantities along curves emanating from the singularity.

Thus, assume that $r(t)$ is a curve such that $r(0) = r_{i+\frac{1}{2}}^n$. Using the previous notation, let $\Lambda = r'(0)$ be its initial slope. If $Q(r, t)$ is any flow variable, its derivative in the direction of $r(t)$ at $t=0$ is given by,

$$\frac{dQ}{dt} = \left(\frac{\partial Q}{\partial t} \right)_0 + \left(\frac{\partial Q}{\partial r} \right)_0 \cdot \Lambda. \quad (3.7)$$

In this equation the derivatives $(\partial Q/\partial t)_0$, $(\partial Q/\partial r)_0$ are obtained from the GRP analysis. More precisely, while $(\partial Q/\partial t)_0$ is directly linked to the solution of the GRP (see Eq. (2.12)), the limiting value of the spatial derivative $\partial Q/\partial r$ at the singularity, denoted in Eq. (3.7) as $(\partial Q/\partial r)_0$, is obtained from corresponding time derivatives via the flow equations (2.10) (compare the discussion preceding Eq. (2.22)). In particular, observe that these derivatives must be interpreted in an appropriate one-sided sense when $r(t)$ is a curve of discontinuity in flow variables (or their derivatives). We refer the reader to Ref. (3) for a more extensive discussion of the ALE analysis. In view of the practical significance of this analysis when applied to the tracking of flow singularities, we consider some aspects of this subject in the next subsection.

3.3 Singularity tracking

As is well known, the tracking of hydrodynamic singularities (shock or contact discontinuities) greatly enhances the accuracy and level of resolution of flow simulations. As discussed in the previous subsection, the GRP analysis, when applied at a given cell boundary, yields full information about the wave structure of the local flow, including directional derivatives along any trajectory emanating from the singularity. Consequently, a "singularity" scheme, of second-order accuracy, is naturally obtained. In particular, grid-points can be made to follow not only jump discontinuities (shocks, contacts) but also paths of secondary waves, such as end characteristics of rarefaction waves.

The resulting grid, whose points (=cell boundaries) we denote by $r_{i \pm \frac{1}{2}}(t)$, comprises an ordered set of fixed Eulerian points, Lagrangian points (following contact discontinuities, material interfaces, etc.) and points assigned to follow various waves (shocks etc.). Thus, every grid-point is assigned a speed $\Lambda_{i \pm \frac{1}{2}}(t) = r'_{i \pm \frac{1}{2}}(t)$. Clearly, $\Lambda_{i \pm \frac{1}{2}} = 0$ for a fixed Eulerian point, while $\Lambda_{i \pm \frac{1}{2}}$ (as well as $(d/dt)\Lambda_{i \pm \frac{1}{2}}(t)$) is obtained from the local GRP analysis for those grid-points assigned to track flow singularities.

The difference scheme is given by Eq. (3.6). In order to maintain second-order accuracy, one must evaluate the time-centered fluxes in Eq. (3.6) by,

$$\begin{aligned} [(\Lambda U - F(U))A]_{i+\frac{1}{2}}^{n+\frac{1}{2}} &= [(\Lambda U - F(U))A]_{i+\frac{1}{2}}^n \\ &+ \frac{1}{2} \Delta t \cdot \frac{d}{dt} [(\Lambda U - F(U))A]_{i+\frac{1}{2}}^n, \end{aligned} \quad (3.8)$$

(compare Eq. (2.7)). The first term in the right-hand side of Eq. (3.8) is obtained from the solution of the associated Riemann problem (see Eq. (2.15)) while

the second term follows from the GRP analysis.

In order to avoid formation of excessively small cells in the grid, an Eulerian grid-point located within a fraction β of cell size from a (moving) neighboring gridpoint is temporarily deleted (typically $\beta=0.25$). The deletion (restoration) of Eulerian grid-points is performed as a “cell-merging” (“cell-splitting”) operation. In cell-merging the conserved variables (density, momentum, energy) are averaged over the merged cell so that total values are conserved. An analogous algorithm is applied in the case of cell-splitting. For full details of the “singularity tracking” method, we refer the reader to Refs. (17), (18).

3.4 Monotonicity algorithm

Following the evaluation of the new cell averages U_i^{n+1} , one must determine the new slopes $(\Delta U)_i^{n+1}$ (see steps (d)–(e) in the description of the numerical procedure given in the beginning of this section).

In fact, one first computes the slopes as a straightforward application of the GRP analysis (see Eq. (3.1)). It should be emphasized that the determination of slopes at this stage is totally independent of the conservative scheme leading to the evaluation of the new cell averages U_i^{n+1} . Indeed, one might argue that the GRP analysis is used (indirectly) in the (numerical) time integration of the evolution equation satisfied by the slope $(\partial/\partial r)U$ (obtained formally by differentiating Eq. (2.1) with respect to r). Note that the discrete slopes $(\Delta U)_i^{n+1}/(r_{i+\frac{1}{2}} - r_{i-\frac{1}{2}})$ approximate $\partial U/\partial r$ with first-order accuracy only.

As has already been observed by van Leer⁽³³⁾, using these slopes with no further modification would lead to unstable computations. Note, in particular, that near large jumps, such slopes may lead to negative values of density at cell boundaries etc. Thus, one must “correct” these slopes by imposing suitable “limiters” on their magnitude, designed, generally speaking, to maintain monotonic behavior of flow profiles across cell boundaries. (This procedure is equivalent to the use of “limiters” in other high-resolution schemes, and at least in the case of a single conservation law, is needed to ensure that the scheme possesses the TVD property).

The philosophy of the GRP scheme is to keep to a minimum all numerical “interventions” not directly related to the GRP analysis. Thus, for our monotonicity algorithm we adopted the basic (and simplest) one introduced by van Lee⁽³³⁾. It can be summarized as follows.

Let Q be any flow variable (pressure, velocity etc.) and let $Q_{i-1}^n, Q_i^n, Q_{i+1}^n$ be the values of its averages in three consecutive cells. Let $Q_{i\pm\frac{1}{2}}^n = Q_i^n \pm (1/2)(\Delta Q)_i^n$ be its values at the boundaries of cell i ,

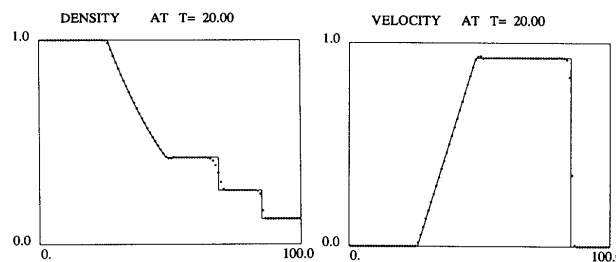


Fig. 3 Sod's shock-tube problem. No tracking

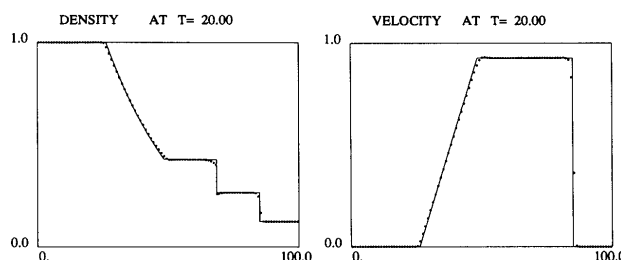


Fig. 4 Sod's shock-tube problem. Tracking of contact

as determined by the unmodified slope $(\Delta Q)_i^n$. Let $(\tilde{\Delta Q})_i^n$ be the modified slope, leading to modified values $\tilde{Q}_{i\pm\frac{1}{2}}^n = Q_i^n \pm (1/2)(\tilde{\Delta Q})_i^n$. Then :

- (a) If Q_i^n is an extremum for the triplet $\{Q_{i-1}^n, Q_i^n, Q_{i+1}^n\}$, then set $(\tilde{\Delta Q})_i^n = 0$.
- (b) Otherwise, $\{Q_{i-1}^n, Q_i^n, Q_{i+1}^n\}$ is a monotonic triplet.

In this case, if $\{Q_{i-1}^n, Q_{i-\frac{1}{2}}^n, Q_i^n, Q_{i+\frac{1}{2}}^n, Q_{i+1}^n\}$ is not monotonic, “tilt” $(\Delta Q)_i^n$ by the minimum amount (i. e., $|\Delta Q)_i^n - (\tilde{\Delta Q})_i^n|$ is as small as possible) needed in order to obtain a monotonic sequence $\{Q_{i-1}^n, \tilde{Q}_{i-\frac{1}{2}}^n, Q_i^n, \tilde{Q}_{i+\frac{1}{2}}^n, Q_{i+1}^n\}$.

Note that under all circumstances the cell averages U_i^{n+1} , as computed by the conservative scheme, are never subject to any modification.

3.5 Sod's example

The well-known shock tube problem proposed by Sod⁽³¹⁾ has served as a standard test case for the evaluation of numerical schemes. We present here our results for this problem, using the basic E_∞ -scheme for a fixed Eulerian grid and two improvements due to an application of the “singularity tracking” technique.

The tube extends from $r=0$ to $r=100$ (with planar symmetry, $A(r)\equiv 1$) and is divided into 100 equal cells. The fluid is a γ -law perfect gas with $\gamma=1.4$. The initial conditions are $u=0, p=\rho=1$ for $0 < r < 50$; $u=0, p=0.1, \rho=0.125$ for $50 < r < 100$.

In Fig. 3 we show the flow profiles at $t=20$ (the exact self-similar solution is given by the solid curve), where the E_∞ -scheme is used to obtain the solution on a fixed Eulerian grid. While a sharp resolution of the

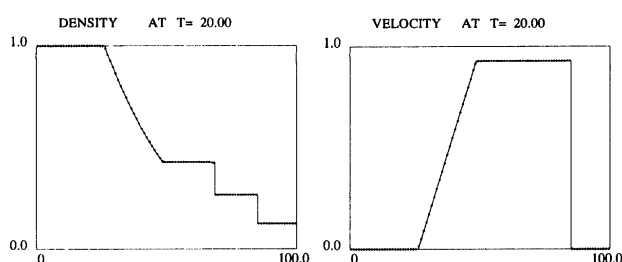


Fig. 5 Sod's shock-tube problem. Tracking of shock, contact and tail of rarefaction

shock wave is obtained, it is seen that the contact discontinuity, as well as the tail characteristic of the rarefaction wave, are less accurately resolved. In Fig. 4, we modify the fixed Eulerian grid by adding the contact discontinuity as a "tracked" grid point, as discussed in subsection 3.3. Clearly, this discontinuity is now sharply resolved, while the profiles near the tail characteristic of the rarefaction wave are unchanged. Finally, in Fig. 5, three grid points, namely, the shock, contact discontinuity and tail characteristic of the rarefaction wave, are all tracked. The improved sharpness of the profiles is evident.

4. Physical Extensions

The philosophy underlying the GRP method can be applied to a variety of nonlinear hyperbolic systems, which extend the basic fluid dynamical system (2.1). A system of special interest is that of reacting flows. In such a system the mass fractions of the various components (depending on space and time) are governed by suitable reaction equations. These equations are coupled with the basic conservation laws, resulting in a nonlinear hyperbolic system which is multiply "linearly degenerate" along the characteristic curve $dx/dt = u$.

We emphasize that the GRP method enables us to treat the fully coupled system, and there is no need to use a "split" algorithm, in which the "fluid dynamical" step is separated from the "chemical" step (compare Ref. (12)). In the following we outline briefly the GRP treatment of

- (a) reacting gas, assuming planar symmetry, and
- (b) reacting gas, in quasi 1-D geometries, where external potentials are also present.

4.1 Combustion

Consider the Euler equations that model the time-dependent flow of an inviscid, compressible, reacting gas. Assuming plane symmetry, and denoting by x the spatial coordinate, the equations can be written in "quasi-conservative" form as

$$\frac{\partial}{\partial t} U + \frac{\partial}{\partial x} F(U) = G(U),$$

$$U = \begin{pmatrix} \rho \\ \rho u \\ \rho E \\ \rho z \end{pmatrix}, \quad F(U) = \begin{pmatrix} \rho u \\ \rho u^2 + p \\ \rho u E + pu \\ \rho zu \end{pmatrix}, \quad (4.1)$$

$$G(U) = \begin{pmatrix} 0 \\ 0 \\ 0 \\ -k(\rho, p, z)\rho \end{pmatrix}.$$

Here ρ, p, E, u are as in Eq. (2.1) and z is the mass fraction of the unburnt gas. Thus $z=1$ ($z=0$) represents the completely unburnt (burnt) gas. Note, however, that the total specific energy $E = e + u^2/2$ contains also the "internal chemical energy", incorporated in the specific internal energy e . The equation of state here takes the form $p = p(e, \rho, z)$. In addition, the fourth equation in (4.1) (to which we refer below as the "chemical" equation) involves a "reaction rate" function $k(\rho, p, z)$. We assume in general that $k > 0$, so that the process is "irreversible". Note that this equation can also be written as

$$\frac{dz}{dt} = -k \text{ along } \frac{dx}{dt} = u. \quad (4.2)$$

As was the case with the system (2.1), one is led to a "quasi-conservative" difference scheme analogous to Eq. (2.3), which in turn gives rise to a GRP algorithm as in Eqs. (2.7)–(2.9). We refer the reader to Ref. (2) for full details concerning the solution to the GRP in this case.

There are two important aspects of Eq. (4.1) which are not present in the case of the fluid dynamical system (2.1), and which have both theoretical and numerical ramifications. These are (a) the significance of the coupling between the fluid dynamical and chemical equations, and (b) the effect of "stiffness" of the chemical equation.

To understand the coupling effect, we need to clarify first the definition of the speed of sound c in our case. To this end, we take e, ρ, z as the basic thermodynamic variables and express the entropy S as a function $S(e, \rho, z)$. The entropy satisfies, for every fixed value of z , the second law of thermodynamics,

$$TdS \equiv T \left(\frac{\partial S}{\partial e} de + \frac{\partial S}{\partial \rho} d\rho \right) = de + p d \left(\frac{1}{\rho} \right). \quad (4.3)$$

Observe that Eq. (4.3) expresses the underlying idea that the whole process involves a "continuum" of fluids, labeled by z . Fixing a value of z , we obtain a "material" which satisfies all the thermodynamic requirements and in particular Eq. (4.3). In Eq. (4.3) the temperature T is assumed to be a known function of (e, ρ, z) .

The function $S = S(e, \rho, z)$ can be inverted to yield $e = e(\rho, S, z)$, and a substitution in $p = p(e, \rho, z)$ gives $p = p(S, \rho, z)$. We then set

$$c^2 = \frac{\partial p}{\partial \rho}(\rho, S, z). \quad (4.4)$$

Remark: We note an interesting mathematical fact related to the basic law of thermodynamics, as expressed by Eq. (4.3). In the “classical” case, as is well known, there are only two independent variables, for example e, ρ . With $p = p(e, \rho)$, one is then looking for a function $T = T(e, \rho) > 0$, such that the expression

$$\frac{1}{T} \left(de + p d\left(\frac{1}{\rho}\right) \right)$$

is a total differential of a functions $S(e, \rho)$. Thus, $1/T$ is an “integrating factor”, which always exists in the two-variable case. However, if three independent variables are assumed (for example e, ρ, z) then such an integrating factor in general does not exist and one can require Eq. (4.3) to hold only for fixed values of z .

To illustrate the above discussion, we specialize to the case of a “ γ -law gas”, where, instead of Eq. (2.2), we now have

$$p = (\gamma - 1)\rho(e - q_0 z), \quad \gamma > 1, \quad q_0 > 0. \quad (4.5)$$

The quantity q_0 is the amount of “chemical” energy released in full burning, $q_0 > 0$ being equivalent to an “exothermic” process.

It is assumed that $\gamma > 1$ is independent of z , for simplicity. A more realistic model, even for ideal gases, assumes some dependence of γ on z .

From our definition of entropy it follows that in this case

$$S = \frac{1}{\gamma - 1} \frac{p}{\rho^\gamma} = \rho^{1-\gamma}(e - q_0 z), \quad (4.6)$$

so that, expressed in terms of $\rho, S, z, p = (\gamma - 1)\rho^\gamma S$, and, by Eq. (4.4).

$$c^2 = \frac{\partial p}{\partial \rho} = \gamma \frac{p}{\rho}. \quad (4.7)$$

It is easily checked that the first three equations of (4.1) yield the characteristic relation

$$\frac{de}{dt} + p \frac{d}{dt} \left(\frac{1}{\rho} \right) = 0 \quad \text{along} \quad \frac{dx}{dt} = u. \quad (4.8)$$

Using Eq. (4.2) and the fourth equation of (4.1) we obtain

$$\begin{aligned} \frac{dS}{dt} &= \frac{\partial}{\partial z} S(e, \rho, z) \frac{dz}{dt} = -k(e, \rho, z) \frac{\partial}{\partial z} S(e, \rho, z) \\ \text{along} \quad \frac{dx}{dt} &= u. \end{aligned} \quad (4.9)$$

In general, the behavior of the reaction rate function k can be quite complex. However, in many cases it suffices to take an “Arrhenius” law, namely,

$$k = Kz\psi(T), \quad K > 0, \quad (4.10)$$

where $\psi(T)$ is a suitable function of the temperature. We refer the reader to Ref. (23), where the GRP is treated with k as given by Eq. (4.10). Here we simplify the model further, and assume that

$$k = KzH(T - T_c), \quad K > 0, \quad T = \frac{p}{\rho}, \quad (4.11)$$

where the Heaviside function H is given by

$$H(y) = \begin{cases} 1, & y > 0, \\ 0, & y \leq 0. \end{cases}$$

Thus, there is no chemical reaction if the temperature does not reach a critical level T_c , beyond which the reaction rate is linearly proportional to the mass fraction z (see Refs. (2) and (12) where Eq. (4.11) is used).

Plugging the simplified model (4.5), (4.11), into the characteristic equation (4.9) leads to

$$\frac{dS}{dt} = -Kq_0\rho^{1-\gamma}zH(T - T_c) \quad \text{along} \quad \frac{dx}{dt} = u. \quad (4.12)$$

Also, the other characteristic relations in this case are given by

$$\begin{aligned} \rho c du \pm dp &= \pm(\gamma - 1)Kq_0\rho zH(T - T_c) \\ \text{along} \quad \frac{dx}{dt} &= u \pm c. \end{aligned} \quad (4.13)$$

We refer the reader to Ref. (2) for a derivation of Eq. (4.13).

Observe that in the absence of a chemical process, the right-hand sides of Eqs. (4.12)–(4.13) vanish identically. On the other hand, if the product Kq_0 is large, it follows that the “Riemann invariants” undergo rapid changes along their respective characteristic curves and there exists strong coupling between the fluid dynamical and the chemical phases of the flow. In this case, a numerical algorithm that splits the two phases can lead to large errors, as we shall see below.

The “stiff” aspect of the chemical equation is a well-known topic in numerical analysis. The basic facts are simple, and can be demonstrated in terms of the linear equation $dy/dt = -Ky$, $K > 0$.

To discretize the equation (whose solution is a decaying exponential) one can use an “explicit” scheme,

$$\frac{y^{n+1} - y^n}{\Delta t} = -Ky^n \quad (4.14)$$

leading to $y^{n+1} = (1 - K\Delta t)y^n$, or an “implicit” scheme,

$$\frac{y^{n+1} - y^n}{\Delta t} = -Ky^{n+1}, \quad (4.15)$$

leading to $y^{n+1} = (1 + K\Delta t)^{-1}y^n$. Clearly, the implicit scheme is stable for all Δt , while the explicit scheme requires $\Delta t < K^{-1}$, which becomes more and more restrictive as K increases, namely, as the equation becomes “stiffer”.

We emphasize that the GRP scheme for Eq. (4.1) does not attempt to resolve the stiffness issue of the system. Thus, in accordance with our general approach, an explicit version of the algorithm is used to handle the chemical equation. We refer the reader to Ref. (2) for full details. In Figs. 6(a), (b) below we show results obtained by using the explicit and implicit schemes. It is shown that the implicit scheme

leads to “non physical” solutions. This numerical effect, related to the combination of a “high-resolution” scheme for the fluid dynamical equations and an “implicit” scheme for the chemical equation, was studied in Ref. (12), where a full “analytic” solution for the chemical equation was used.

Before presenting the numerical results for Eq. (4.1), we recall briefly the structure of a C-J detonation wave in the Z-N-D model for the solutions of the system (see Ref. (13) for details). The wave (corresponding to C-J sharp front in the Chapman-Jouguet theory) consists of a reaction zone of finite width moving at the C-J speed, across which the mass fraction z varies from $z=1$ to $z=0$. The edge of the reaction zone facing the unburnt ($z=1$) gas is a fluid-dynamical shock wave which raises the pressure and density to values significantly higher than the C-J values. We refer to this shock at the “Z-N-D spike”. Following the spike, the pressure and density drop monotonically and continuously to their C-J values at the other edge of the reaction zone.

As a test case let us consider the ozone decomposition discussed in Refs. (2) and (12). The equation of state is given by Eq. (4.5) (in CGS units), and the reaction rate by Eq. (4.11) where

$$\gamma=1.4, \quad q_0=0.5196 \cdot 10^{10}, \\ K=0.5825 \cdot 10^{10}, \quad T_c=0.1155 \cdot 10^{10}.$$

The initial data was taken as the piecewise constant data defining a C-J detonation as a single wave (recall that such a wave in the Chapman-Jouguet theory is a sonic detonation). The initial state was given by

$$(p, \rho, u, z) = \begin{cases} 8.321 \cdot 10^5, 1.201 \cdot 10^{-3}, 0, 1 & x > 50\Delta x, \\ 6.270 \cdot 10^6, 1.945 \cdot 10^{-3}, 4.162 \cdot 10^4, 0, & x < 50\Delta x. \end{cases}$$

In Figs. 6(a), (b), we give the results for the explicit and implicit calculations, respectively. We have used 100 cells with $\Delta x = 5 \cdot 10^{-5}$ cm. In this case, the reaction zone is of roughly the same size as one computational cell. It is seen that the explicit scheme (which is the one used in the GRP scheme) produces a Z-N-D spike moving at the right speed (the spike is truncated since the reaction zone is now averaged out over the cell). On the other hand, the implicit scheme produces a non physical weak detonation wave (which is supersonic with respect to the flow behind it) followed by an “adjusting” fluid dynamical shock wave in the totally “burnt” (i.e., in our case, the totally decomposed ozone) gas. Observe that such a solution, while not satisfying the entropy condition (or the “geometrical Lax condition”, since it involves a shock wave which is supersonic with respect to both sides) is still a valid “weak solution” of Eq. (4.1). We have here an interesting example of the interplay between the numerical algorithm and the theoretical aspects of stiffness and non uniqueness for solutions of Eq. (4.1). Thus, if Δx is increased, the reaction zone is absorbed in a fraction of a cell and the spike is (almost entirely) “clipped”. This has the same effect as that of increasing the reaction coefficient K (thus narrowing the reaction zone in the profile). As the discussion following Eq. (4.15) indicates, this in turn results in total burning (i.e., transition from $z=1$ to $z=0$) of a cell in one time-step Δt . The speed of the resulting detonation wave is $\Delta x/\Delta t$. Such a speed is achieved as that of a suitable weak detonation (selected from the one-parameter family of such solutions) with a trailing fluid-dynamical shock.

We refer to Ref. (9) for a different approach to the GRP problem in this case, and to Ref. (25), where a simplified model of combustion is studied theoretically and numerically, using a GRP approach.

4.2 Combustion with external potentials, in quasi 1-D geometries

As was the case in Eq. (2.1), we can formulate

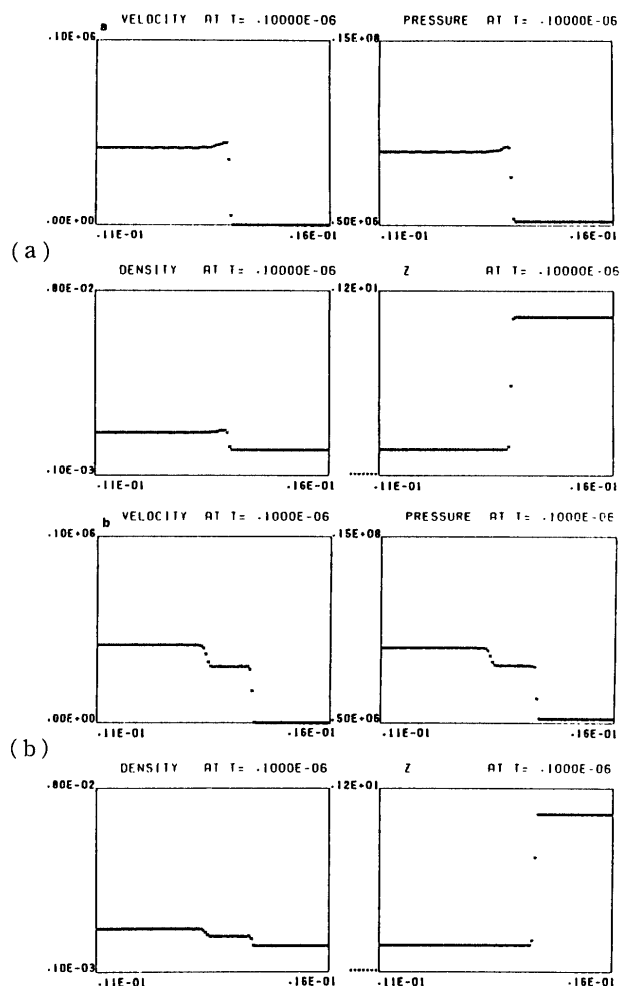


Fig. 6 (a) C-J wave, explicit scheme (b) C-J wave, implicit scheme (Reaction zone ≈ 1 cell)

the conservation laws of compressible flow through a duct of smoothly varying cross-section, when this flow involves chemical reactions and is also subject to external potentials. Such equations occur in astrophysical studies, where spherical symmetries (stars, gas clusters, etc.) are quite natural. In such cases the external potential represents gravity forces, and the chemical equations can be quite general (see Ref. (4) and references therein).

Denoting by r the spatial coordinate, by $A(r)$ the area of the cross-section at r and by $\phi(r)$ the external potential, and using all other notations as in Eq. (4.1), the equations can be written as

$$A(r)\frac{\partial}{\partial t}U + \frac{\partial}{\partial r}(AF(U)) + A\frac{\partial}{\partial r}G(U) + AH(U) = 0, \quad (4.16)$$

$$U = \begin{pmatrix} \rho \\ \rho u \\ \rho E \\ \rho z \end{pmatrix}, \quad F(U) = \begin{pmatrix} \rho u \\ \rho u^2 \\ (\rho E + p)u \\ \rho zu \end{pmatrix}, \quad G(U) = \begin{pmatrix} 0 \\ p \\ 0 \\ 0 \end{pmatrix},$$

$$H(U) = \begin{pmatrix} 0 \\ \rho\phi'(r) \\ 0 \\ k\rho \end{pmatrix}.$$

We refer the reader to Ref. (4), where the GRP scheme for Eq. (4.16) is discussed and various examples are presented, including the computation of spherical "Taylor profiles".

Another interesting case of a two-phase flow in quasi 1-D geometry was studied by Wang and Wu⁽³⁴⁾. In their case the two phases consist of an ideal (compressible) gas phase and a particle (suspension) phase. Physical effects, such as heat transfer between the phases, are treated as "source terms" in the extended nonlinear system, and, as in the case of external potentials, are included in the analogue of the vector $H(U)$ in Eq. (4.16).

5. Two-Dimensional Extensions

5.1 Operator splitting

In constructing a two-dimensional scheme for time-dependent compressible flow, we exploit a well-known technique of operator splitting as proposed by Strang⁽³²⁾. An outline of the method and the key ideas are presented below. The equations governing compressible flow of an inviscid fluid in two space dimensions in conservation form are

$$\frac{\partial}{\partial t}U + \frac{\partial}{\partial x}F(U) + \frac{\partial}{\partial y}G(U) = 0, \quad (5.1)$$

$$U(x, y, t) = \begin{bmatrix} \rho \\ \rho u \\ \rho v \\ \rho E \end{bmatrix}, \quad F(U) = \begin{bmatrix} \rho u \\ \rho u^2 + p \\ \rho uv \\ (\rho E + p)u \end{bmatrix},$$

$$G(U) = \begin{bmatrix} \rho v \\ \rho uv \\ \rho v^2 + p \\ (\rho E + p)v \end{bmatrix},$$

where ρ, p, E are as in Eq. (2.1), and (u, v) are the velocity components corresponding to the Cartesian coordinates (x, y) .

Operator splitting is obtained by decomposing the spatial operator in Eq. (5.1) into two one-dimensional operators in the following manner.

$$\begin{aligned} \frac{\partial U}{\partial t} + (A+B)U &= 0, \\ AU &= -\frac{\partial}{\partial x}F(U), \\ BU &= -\frac{\partial}{\partial y}G(U), \end{aligned} \quad (5.2)$$

leading to splitting of the single two-dimensional conservation system into a set of two one-dimensional systems, as follows.

$$\begin{aligned} (a) \quad \frac{\partial}{\partial t}U^{(1)} + AU^{(1)} &= 0, \\ (b) \quad \frac{\partial}{\partial t}U^{(2)} + BU^{(2)} &= 0. \end{aligned} \quad (5.3)$$

Let $S(t)$ be the solution operator for Eq. (5.2), i.e., for a given initial condition $U_0 = U(x, y, 0)$ the solution to Eq. (5.2) is given by $U(x, y, t) = S(t)U_0$. Similarly, let $S^{(1)}(t)$, $S^{(2)}(t)$ be the solution operators to Eqs. (5.3) (a), (5.3) (b), respectively. Then Strang⁽³²⁾ has shown that if $L^{(1)}(\Delta t)$, $L^{(2)}(\Delta t)$ are second-order accurate finite-difference approximations to $S^{(1)}(\Delta t)$, $S^{(2)}(\Delta t)$, respectively, the operator

$$L(\Delta t) = L^{(1)}\left(\frac{\Delta t}{2}\right)L^{(2)}(\Delta t)L^{(1)}\left(\frac{\Delta t}{2}\right) \quad (5.4)$$

is a second-order accurate finite-difference approximation to $S(\Delta t)$.

Observe that to within second-order accuracy

$$\begin{aligned} L(2\Delta t) &= L^{(1)}\left(\frac{\Delta t}{2}\right)L^{(2)}(\Delta t)L^{(1)}\left(\frac{\Delta t}{2}\right) \\ &\quad \times L^{(1)}\left(\frac{\Delta t}{2}\right)L^{(2)}(\Delta t)L^{(1)}\left(\frac{\Delta t}{2}\right) \\ &= L^{(1)}\left(\frac{\Delta t}{2}\right)L^{(2)}(\Delta t)L^{(1)}(\Delta t)L^{(2)}(\Delta t)L^{(1)}\left(\frac{\Delta t}{2}\right), \end{aligned} \quad (5.5)$$

which implies that in the sequence of operators corresponding to $L(n\Delta t)$, all but the first and last ones are whole-step operators.

Given an Eulerian rectangular grid (in the x - y plane), the operators $L^{(1)}$ and $L^{(2)}$ are obtained as in Section 2 above. Thus, we assume that in every computational cell all flow variables have constant x and y derivatives. In implementing $L^{(1)}$ (the "x-sweep") we ignore all y -derivatives, thus obtaining a conservative scheme in the x -direction. This scheme is used in the evaluation of the fluxes in the x -direction (i.e., across the sides parallel to the y -axis). The

updated values obtained in this way serve as initial values for the following “ y -sweep” (implementation of $L^{(2)}$). At each step, the monotonicity algorithm is applied. The reader is referred to Refs. (14)–(16) for more details. However, it is emphasized here that while each of the operators $L^{(1)}$, $L^{(2)}$ is obtained by the GRP guidelines, the split scheme (5.4) follows the standard application of the Strang scheme. In particular, one can use for $L^{(1)}$ and $L^{(2)}$ the basic E_1 -schemes (see Section 3.1 above). Observe that the third equation in (5.1), gives rise, by Eq. (5.3) (a), to a conservation equation for the transverse momentum components, namely

$$\frac{\partial}{\partial t}(\rho v) + \frac{\partial}{\partial x}(\rho uv) = 0. \quad (5.6)$$

This equation is a pure advection of v along the one-dimensional “particle path” $dx/dt = u$. In this respect, the quantity v is analogous to the mass fraction z discussed in the previous section.

Some examples using this scheme are outlined in the following section.

5.2 Moving boundary tracking (MBT)

Numerous physical and engineering applications call for the computation of time dependent compressible flows involving interaction with a moving impermeable surface. Assuming in our case that the motion of any such surface is given as a function of time, the MBT scheme is designed to compute the evolving flow in two space dimensions. In the following, we provide a brief outline of this scheme and its key ideas. A more detailed account of MBT can be found in Ref. (15).

The MBT scheme consists of the split 2-D GRP scheme outlined above, in conjunction with several modifications which are needed in the partial cells formed by the intersection of the moving boundary surface with the underlying Cartesian grid. In keeping with the spirit of operator splitting, the motion of the tracked boundary is also split into x , y displacement components, which are treated separately at the respective split integration phase.

We illustrate the principles of MBT by concentrating on a representative part of the entire scheme, namely the $L^{(1)}(\Delta t)$ integration (as noted in Eqs. (5.4), (5.5) above) of the mass conservation law. Furthermore, we restrict the discussion to the typical boundary configuration depicted in Fig. 7.

The finite-difference approximation to the first equation of (5.3) (a) is given by (compare Eq. (2.3)),

$$\rho_i^{n+1} = \frac{1}{V_i^{n+1}} \left\{ \rho_i^n V_i^n - \Delta t \left[A_{i+\frac{1}{2}}^{n+\frac{1}{2}} (\rho u)_{i+\frac{1}{2}}^{n+\frac{1}{2}} - A_{i-\frac{1}{2}}^{n+\frac{1}{2}} (\rho u)_{i-\frac{1}{2}}^{n+\frac{1}{2}} \right] \right\} \quad (5.7)$$

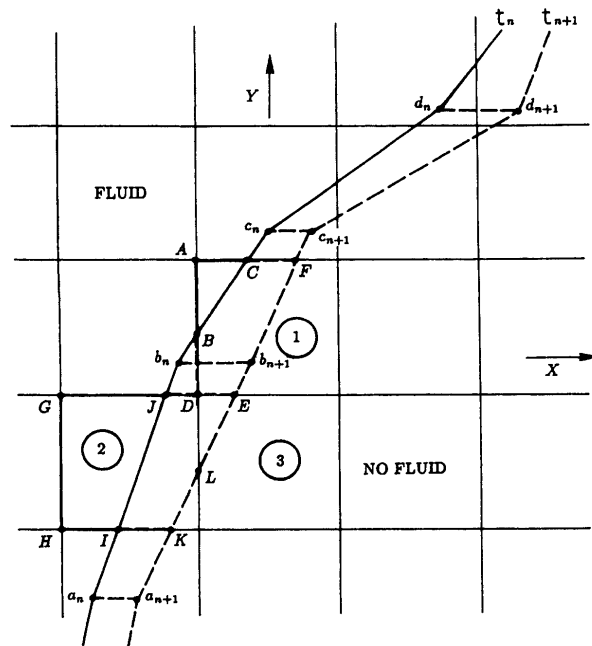


Fig. 7 x -split phase of moving boundary tracking

where $\Delta t = t_{n+1} - t_n$, and V_i^n , V_i^{n+1} are, respectively, the areas of cell i at t_n , t_{n+1} . Note that for the sake of simplicity we use here a single subscript “ i ” to denote a cell in the two-dimensional grid. As in Eq. (2.3) the subscripts $i \pm 1/2$ refer to left and right segments of the cell-boundary, having lengths $A_{i \pm 1/2}^{n+\frac{1}{2}}$. These lengths are appropriate time-averaged values related to the detailed motion of the boundary. Similarly, $(\rho u)_{i \pm 1/2}^{n+\frac{1}{2}}$ are time-averaged values of the mass flux across the respective cell-boundary segments.

As specific cases of boundary cells, highlighting features of the MBT scheme, we consider Cell 1 and Cell 2 in Fig. 7. Cell 1 is a relatively simple case: $A_{i+\frac{1}{2}}^{n+\frac{1}{2}} = 0$ and the sole intricate task is to evaluate $A_{i-\frac{1}{2}}^{n+\frac{1}{2}}$. At t_n the exposed face is AB and at some intermediate moment $t_n < t_{n+\alpha} < t_{n+1}$ ($0 < \alpha < 1$) point D becomes exposed. We then take as the approximate average length the weighted sum

$$A_{i-\frac{1}{2}}^{n+\frac{1}{2}} = \frac{1}{2} \alpha [\text{Length}(AB) + \text{Length}(AD)] + (1-\alpha) \text{Length}(AD).$$

The flux $\rho u_{i-\frac{1}{2}}^{n+\frac{1}{2}}$ is determined in the usual manner for the 1-D GRP scheme by solving the generalized Riemann problem centered about cell-interface $i - 1/2$.

Turning to Cell 2, we encounter a new type of complexity: the neighboring cell, Cell 3, is newly

exposed during the time interval t_n, t_{n+1} . Evidently, no flux can reasonably be computed for the newly exposed face DL . This case is appropriately dealt with by merging new Cells 2 and 3, while the old Cell 2 is identical to the corresponding old polygon. Subsequently, the mass density ρ_i^{n+1} thus evaluated, is assigned as the new density of both Cell 2 and Cell 3.

5.3 Material interface tracking (MIT)

The method of material interface tracking (MIT) is designed to enable a multi-material, fully Eulerian calculation, using the split GRP scheme as described above.

Material interfaces in complex flows can break up or rejoin in an arbitrary fashion. Thus, an accurate tracking of boundaries, using the MBT algorithm as described above (subsection 5.2), is not possible for all practical purposes. (See Ref. (28), where full boundary tracking is used, though only for "Eulerian-Lagrangian" boundaries.)

We refer the reader to Ref. (16) for an account of the MIT scheme. The key idea is basically to forsake the accurate boundary condition at a material interface, replacing it by a simulated (approximate) one. Cells intersected by the interface are, in some sense, treated as though they contain a heterogeneous mixture of fluids. By that we mean that the fluid in multi-material cells is assumed to have uniform pressure and velocity, thereby imposing a "no-slip" boundary condition (instead of a mere continuity of the normal component of velocity). The distinct identity of each fluid is maintained, however, for computing the fluxes of conserved quantities (separately for each fluid).

6. Examples

6.1 Nozzle flow

Consider a typical over-expanded (steady) flow of a compressible inviscid fluid in a converging-diverging nozzle. The flow field is characterized by Mach number $M < 1$ in the converging section, $M = 1$ at the throat (minimal cross-section area), $M > 1$ downstream of the throat, then it jumps to $M < 1$ at a shock located before the exit plane. An exit Mach number $Me < 1$, ensures matching of pressure, i.e., the exit flow pressure is equal to the ambient pressure. It is commonly assumed (as the duct-flow approximation), that this flow is governed by the one-dimensional equations (2.1). In this example we apply the GRP scheme (2.3) to the computation of over-expanded nozzle flow, obtaining a nearly steady solution at large times.

The nozzle extends through the interval $-1 < x < 1$, which is divided into 100 cells. The cross-section area function is taken as

$$A(x) = \exp \left\{ \frac{1}{2} \log (4.2346) [1 - \cos (\pi x)] \right\}.$$

For a perfect gas having $\gamma = 1.40$, this area would produce an exit Mach number $Me = 3$, when ambient pressure is low enough to enable supersonic flow at the nozzle exit. The initial conditions are $u(x, 0) = 0$, $p(x, 0) = 0.5$, $\rho(x, 0) = 0.5$, where u, p, ρ are velocity, pressure and density, respectively.

The boundary conditions (BC) deserve special attention, as they in effect enable simulation of an actual nozzle flow, without explicitly incorporating the flow upstream of the nozzle entrance and downstream of the nozzle exit into the mathematical model.

The inflow BC (at $x = -1$) is designed to simulate a chamber feeding the nozzle with flow having constant stagnation conditions $P_0 = 1$, $\rho_0 = 1$. The boundary point ($x = -1$) is treated as an internal point in the GRP scheme, i.e., fluxes of mass, momentum and energy are computed from the solution to a local generalized Riemann problem. However, for the boundary point, the required GRP data are available only on the inner (right) side, i.e., u_R, P_R, ρ_R and the respective spatial gradients. The BC scheme consists of specifying the corresponding data on the external (left) side of the boundary point. The following scheme was found to simulate given stagnation inflow conditions. We set all spatial gradients to zero, since they are nearly zero within the nozzle at steady flow. The pressure is taken to be continuous, $P_L = P_R$, then u_R, ρ_R are evaluated from standard relations for steady isentropic flow, so that the inflow stagnation pressure and density are equal to the given P_0, ρ_0 .

The outflow BC (at $x = 1$) is designed to simulate a prevailing ambient pressure $P_a = 0.5$. Again, spatial gradients of u, p, ρ are set equal to zero. The pressure is set equal to the ambient pressure $P_R = P_a$, and the velocity and density are taken to be continuous $u_R = u_L, \rho_R = \rho_L$.

The results at $t = 10$, where the flow was seemingly steady, are shown as spatial distribution of pressure and Mach number in Fig. 8. We note that the Mach number distribution agrees with the description given above, and in particular that $M = 1$ at the throat ($x = 0$) and M jumps from $M > 1$ to $M < 1$ at the shock. Also, the pressure distribution exhibits agreement with both boundary conditions. At the nozzle inlet ($x = -1$), the pressure $P \approx P_0$ (since there ($M \ll 1$), and at the nozzle exit ($x = 1$) $P = P_a$, i.e., the exit pressure matching condition is obtained.

A different type of nozzle flow is the interaction of shock waves or rarefaction waves with a smooth area - change segment separating two long ducts of uniform cross - section. A GRP computational

analysis of such flows was performed and is presented in Ref. (22).

6.2 Exploding helium sphere

This computational example was originally suggested by Saito and Glass⁽³⁰⁾. A high-pressure helium bubble is surrounded by air, both are taken to be perfect gases with $\gamma=5/3$ and $\gamma=7/5$, respectively. The initial conditions for u, p, ρ (velocity, pressure, density) are $u=0$ everywhere, $p=18.25$ and $\rho=2.523$ in the helium, $p=1$ and $\rho=1$ in the air. The computation takes place in the domain ($0 \leq x \leq 10$), where the helium occupies the interval ($0 < x < 2.5$). The uniform cell size is $\Delta x=0.1$. The boundary condition at $x=0$ and at $x=10$ is zero velocity ($u=0$).

The computation is performed by the singularity tracking scheme GRP/ST presented in Section 3.3 above. We track three singularity points: the tail characteristic of the rarefaction propagating into the

helium, the helium/air interface point and the air shock. The results are shown at times $t=0.60$ (Fig. 9 (a)) and $t=2.40$ (Fig. 9(b)). Both density and velocity spatial distributions are shown.

At $t=0.60$ the shock and interface discontinuities are clearly visible on the density plot, whereas the velocity plot exhibits solely the shock discontinuity. Also, the tracked tail of the rarefaction is clearly visible as a "corner", i.e., a point of discontinuity in flow gradients. At $t=2.40$ a second (converging) shock has appeared. This shock results from an over-expansion of the helium sphere. It was computed as a captured shock, but as it caught up with the tracked gradient discontinuity (a sound wave), its computation automatically reverted to a tracked shock mode, so that at $t=2.40$ it appears as a perfectly sharp discontinuity. (See Refs. (3), (17) for more details).

6.3 Accelerated piston

A piston initially at $x=0$, is accelerated from rest with constant acceleration $a=0.02465$ driving a compression wave into a quiescent perfect gas ($\gamma=1.40$, pressure and density $p_0=1, \rho_0=1$). The computation domain is ($0 \leq x \leq 100$) and is divided into 100 equal cells. An exact solution is available to this classical problem (Ref. (24), p.382), up until the moment of initial shock formation given by $t_c=2c_0/a(\gamma+1)$, where $c_0=\sqrt{\gamma p_0/\rho_0}$. Using the GRP/ST scheme (Section 3.3 above) to obtain the moving piston boundary

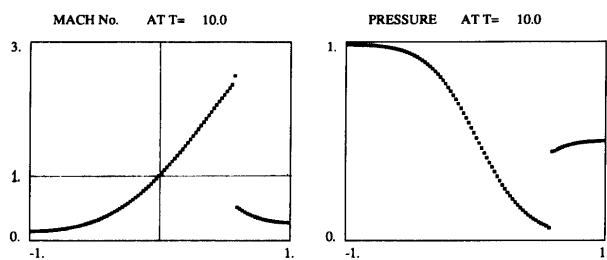


Fig. 8 Steady flow with shock in a converging-diverging nozzle

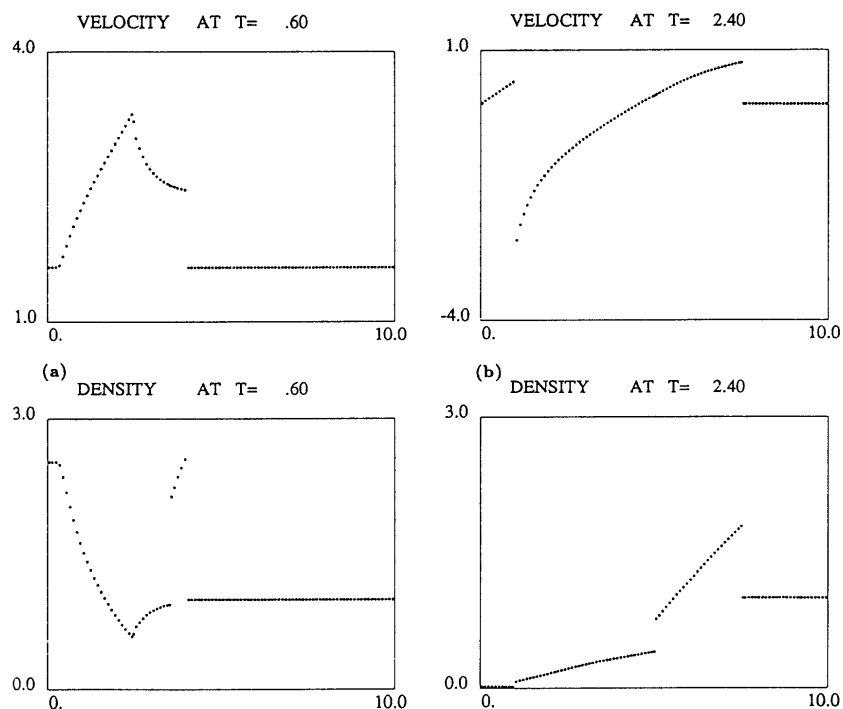


Fig. 9 Exploding helium sphere in air. Pressure ratio 18.25, density ratio 2.5. Computation by GRP/ST scheme. (a) $t=0.60$, (b) $t=2.40$

condition, we performed two computations: one in which the formed shock was computed as a captured shock, and one in which the shock was tracked by initially tracking the leading characteristic of the compression wave. Spatial distributions of the pressure are presented.

In Fig. 10(a) we show the numerical solution together with the exact one (smooth line), at the moment of shock inception $t=40$. The agreement between the numerical and the exact solutions is nearly perfect. At the later time $t=60$, no exact solution is available. Here we compare the untracked solution (Fig. 10(b)) to the tracked one (Fig. 10(c)). Note that the captured shock is spread over one to two cells, whereas the tracked one is a perfectly sharp discontinuity.

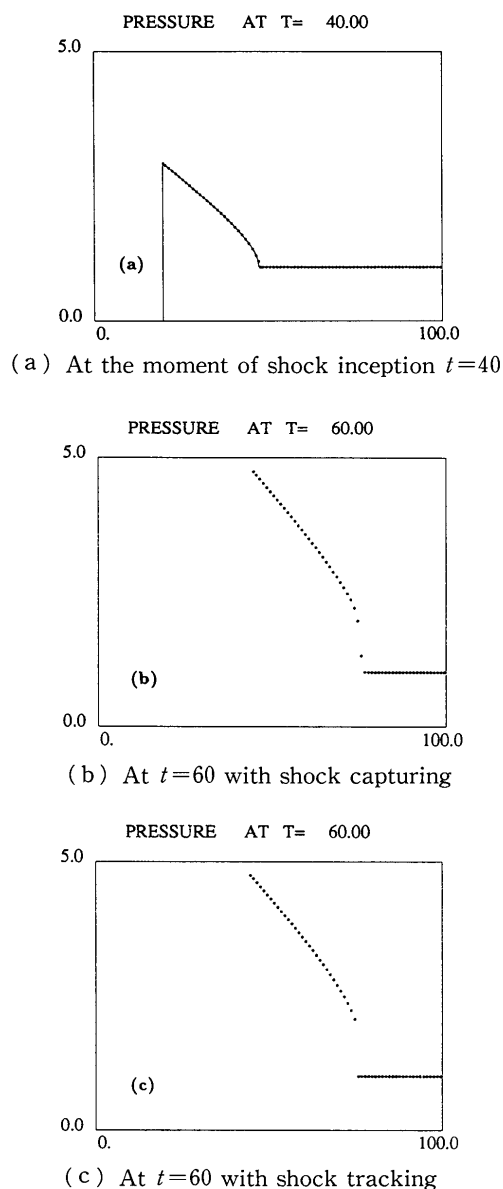


Fig. 10 Piston with constant acceleration

6.4 Shock diffraction at an expansive 90° corner

The two-dimensional diffraction of a planar shock wave by an expansive 90° corner gives rise to a variety of fluid dynamical phenomena that have been the subject of numerous experimental and theoretical studies. Our example is taken from a computational study by Hillier⁽²¹⁾, who used a GRP scheme with an operator splitting as in Section 5.1 above. The cartesian coordinates are (x, y) and the corner point is $(0, 0)$ with the negative parts of the x -axis and the y -axis forming the corner edges. The fluid (taken as perfect gas with $\gamma=1.403$) occupies the quadrant $(x < 0, y > 0)$ and the half-space $(x > 0)$. The mesh size is $\Delta x = \Delta y = 0.008$. The shock is initially located at the corner (the line $x=0$) and its Mach number is $M_s=2.5$. The initial conditions for velocity, pressure, density (u, P, ρ) are: at $(x > 0)$ $u=u_1=0, P=P_1=1, \rho=\rho_1=1$. At $(x < 0, y > 0)$ $u=u_2, P=P_2, \rho=\rho_2$, where u_2, P_2, ρ_2 are the post-shock flow variables corresponding to $M_s=2.5$ and the pre-shock variables u_1, P_1, ρ_1 . The boundary conditions are $u=0$ on the y -axis ($x=0, y < 0$) and $v=0$ on the x -axis ($x < 0, y=0$). On the left boundary of the quadrant ($x < 0, y > 0$), the flow is prescribed as the post-shock flow u_2, P_2, ρ_2 . Since the post-shock flow is supersonic relative to the corner, this latter boundary can be taken as near to the corner as desirable, without affecting the results of the computation.

Density contours are presented in Fig. 11, with an increment of $\Delta \rho = 0.02 \rho_2$. The time is $t=0.8443$, which corresponds to the location $x_s=2.5$ for the

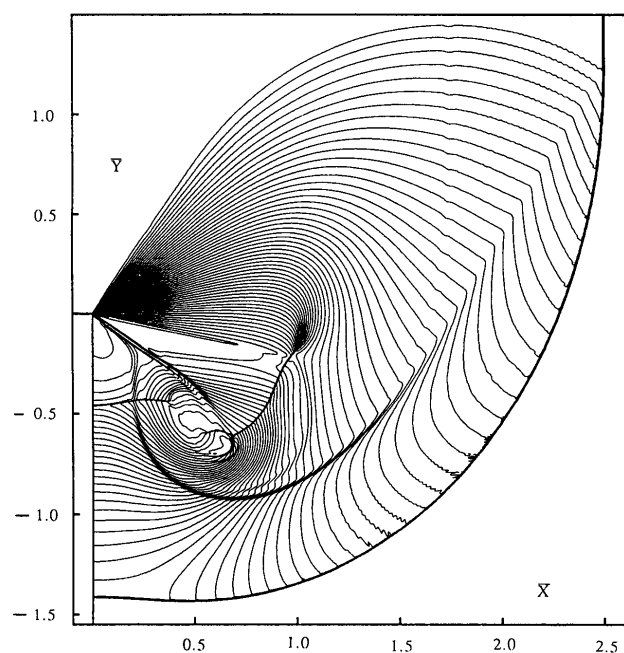


Fig. 11 Diffraction of $M_s=2.5$ shock at a 90° expansive corner. Density contours with $\Delta \rho = 0.02 \rho_2$

incident shock. From Fig. 11 it is apparent that the diffracted shock has moved along the y -axis at speed roughly 75% that of the incident shock. This is an indication of a substantial drop in the post-shock pressure, due to the flow around the corner. Indeed, the density contours at the corner have the typical centered-fan structure of a steady supersonic flow deflected by an expansive corner, which is always accompanied by a reduction in pressure. Moreover, this pressure drop gives rise to the S -shape shock (located midway between the corner and the diffracted shock) which brings about a match between the pressure in the corner-deflected stream and the pressure in the fluid compressed by the diffracted curved shock.

An interesting piece of information was reported by Hillier⁽²¹⁾ concerning the E_1 scheme (Section 3.1 above) which he used. Only 1% of the generalized Riemann problems solved required the more accurate (and computationally intensive) scheme E_∞ .

6.5 Interaction of regular reflection with a compressive corner

The subject of this example is shock reflection by a particular kind of double wedge, where the second wedge surface is parallel to the incident shock (in the experiments the second wedge was simply part of the shock tube endwall). This reflection was studied both numerically and experimentally, and as reported in Ref. (14), a good agreement was obtained between computed and experimental data. The computation was performed by means of the GRP/MBT scheme (Section 5.2 above), where the oblique wedge wall was simulated by a stationary boundary surface.

Here we present the following example taken

from Ref. (14). The incident shock Mach number was $M_s=1.491$, and the wedge angle $\theta=55^\circ$. The fluid in the experiment was dry air at ambient pressure, and it is taken as a perfect gas having $\gamma=1.40$. The computational domain is a rectangle of 11.2×15.0 cm, and it is divided into a mesh of 525×705 square cells. The wedge starts at the midpoint $(5.60, 0)$, and the shock is initially located several cells before that point. The initial conditions ahead of the shock are $u = u_1 = 0$, $P = P_1 = 0.1$ [MPa], $\rho = \rho_1 = 0.0012$ [g/cm³]. After the shock $u = u_2$, $P = P_2$, $\rho = \rho_2$, where u_2 , P_2 , ρ_2 correspond to the post-shock flow variables, derived from $M_s=1.491$ and u_1 , P_1 , ρ_1 as above. The boundary conditions are $v=0$ on the lower and upper walls ($y=0$, $y=15.0$), $u=0$ at the endwall ($x=11.2$) and $(u, P, \rho) = (u_2, P_2, \rho_2)$ at the inflow boundary ($x=0$). The time at which results are shown was chosen by matching the position of the computed head-on reflected shock to the experimental one.

In Fig. 12(a) the experimental interferogram is reproduced. It is estimated that density increment between consecutive lines was $\Delta\rho=0.043\rho_2$, and thus the computed density contours were also calculated with that value of $\Delta\rho$. A good agreement is observed between computed density contours in Fig. 12(b) and the experimental interferogram. All the shock fronts and sliplines observable in the interferogram are also present in the computed density contour map, with a reasonable agreement in shape and location. Moreover, if we examine line counts we also obtain a reasonable agreement. Take, for instance, the region bounded by the lower curved shock, the slip surface and the wedge. There are 10 experimental fringes and 11 computed density contour lines in that region,

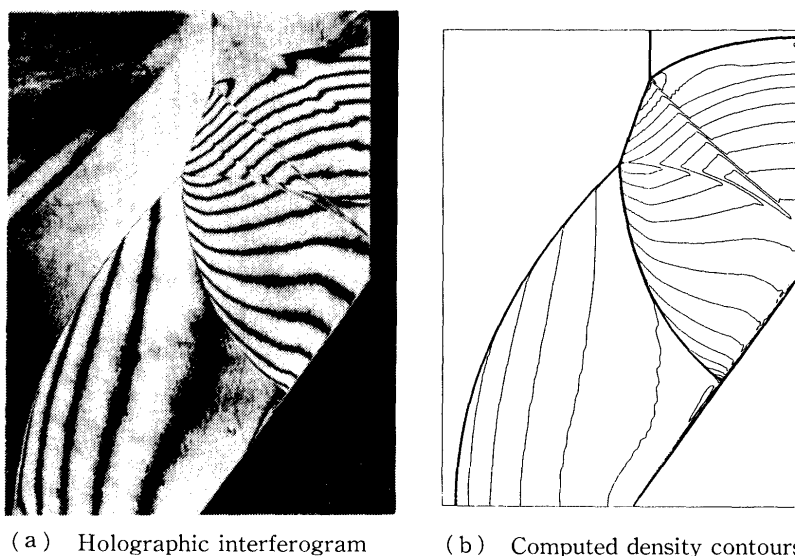


Fig. 12 Shock diffraction by a second wedge parallel to incident shock. Incident shock $M_s=1.491$, wedge angle $\theta=55^\circ$, Density increment $\Delta\rho=0.043\rho_2$

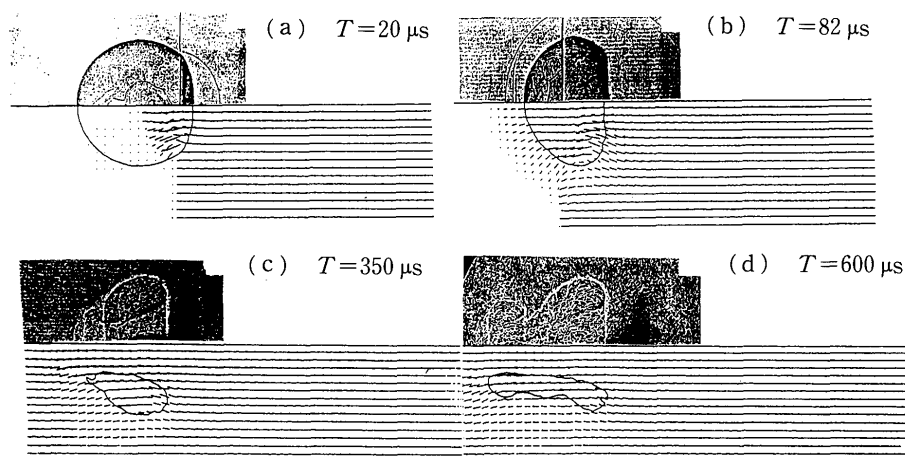


Fig. 13 Interaction of $M_s=1.25$ air shock with a spherical helium bubble

which is a fairly good agreement.

6.6 Interaction of an air shock with a spherical helium bubble

The interaction of a planar air shock wave with a bubble of gas having different acoustic impedance generates a strong vorticity at the interface, leading to bubble breakup and subsequent mixing. The breakup process in such interactions was studied experimentally by Haas and Sturtevant⁽²⁰⁾, who recorded shadowgraphs at a sequence of time points. The air shock Mach number was $M_s=1.25$ and the helium bubble diameter was 4.5 cm. Their experimental results are compared in Figs. 13(a)-(d) with the corresponding computations, which were performed by means of the GRP/MIT scheme outlined in Section 5.3 above.

The computation domain was the rectangle ($0 < x < x_1$, $0 < y < y_1$) with $x_1=27$ cm, $y_1=9$ cm, and it was divided into 270×90 square cells. The center of the spherical helium bubble was initially at (13.5, 0) (only half a circle). Ahead of the shock the pressure was $p=P_1=0.1$ [MPa] everywhere, the air density was $\rho=\rho_1=1.20 \times 10^{-3}$ [g/cm³], the helium density was $\rho_h=(4/29)\rho_1$, and the velocity was $u=u_1=0$, $v=0$ everywhere. The initial location of the shock was (11.25, 0) (it was tangent to the sphere of radius 2.25), and the post-shock initial conditions were $u=u_2$, $v=0$, $P=P_2$, $\rho=\rho_2$, which were obtained as the post-shock values corresponding to $M_s=1.25$ and the pre-shock state u_1 , P_1 , ρ_1 given above. The helium and air were taken to be perfect gases, with $\gamma=5/3$ and $\gamma=7/5$, respectively.

At $t=20 \mu s$ (Fig. 13(a)), the computation (velocity arrows) shows that the shock within the bubble has traversed a much larger distance than the shock in air (apparent on the shadowgraph). At $t=82 \mu s$ (Fig. 13(b)), the incident air shock has just passed the bubble center, and a curved shock transmitted through the bubble into the air is apparent on both the

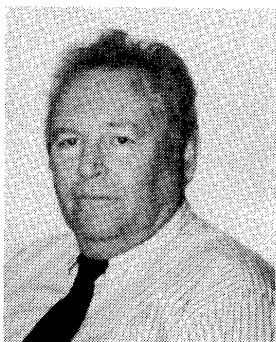
shadowgraph and the computation, with good agreement between the two. There is also good agreement between computed and observed interfaces. At $t=350 \mu s$ (Fig. 13(c)), the bubble has already become a torus, and a good agreement between the computed and shadowgraph interfaces is noted. This agreement persists to $t=600 \mu s$ (Fig. 13(d)), although the shadowgraph is already blurred at that late time, possibly due to onset of diffusion.

This example demonstrates the capabilities of the GRP/MIT scheme, both in terms of accuracy and topological flexibility.

References

- (1) Ben-Artzi, M., The Generalized Riemann Problem in Compressible Duct Flow, *Contemporary Mathematics* (Ed. Keyfitz, B.), Vol. 60 (1987), p. 11.
- (2) Ben-Artzi, M., The Generalized Riemann Problem for Reactive Flows, *J. Comput. Phys.*, Vol. 81 (1989), p. 70.
- (3) Ben-Artzi, M. and Birman, A., Application of the "Generalized Riemann Problem" Method to 1-D Compressible Flows with Material Interfaces, *J. Comput. Phys.*, Vol. 65 (1986), p. 170.
- (4) Ben-Artzi, M. and Birman, A., Computation of Reactive Duct Flows in External Fields, *J. Comput. Phys.*, Vol. 86 (1990), p. 225.
- (5) Ben-Artzi, M. and Falcovitz, J., A Second-Order Godunov-Type Scheme for Compressible Fluid Dynamics, *J. Comput. Phys.*, Vol. 55 (1984), p. 1.
- (6) Ben-Artzi, M. and Falcovitz, J., A High-Resolution Upwind Scheme for Quasi 1-D Flows, in "Numerical Methods for the Euler Equations of Fluid Dynamics", Eds. Angrand, F., Dervieux, A., Desideri J. A. and Glowinski, R., (1985), p. 66, SIAM Publ.
- (7) Ben-Artzi, M. and Falcovitz, J., An Upwind Second-Order Scheme for Compressible Duct Flows, *SIAM J. Sci. Stat. Comp.*, Vol. 7 (1986), p. 744.

- (8) Ben-Artzi, M. and Falcovitz, J., GRP — an Analytic Approach to High Resolution Upwind Schemes for Compressible Fluid Flow, in "Proc. of the 9th Int. Conf. on Numerical Methods in Fluid Dynamics" (Ed. Soubbaramayer and Boujot), Springer Lecture Notes in Physics 218, (1985), p. 87, New York.
- (9) Bourgeade, A., Second-Order Scheme for Reacting Flows — Application to Detonation, Centre d'Etude de Limeil - Valenton, CEA - N - 2570, (1988).
- (10) Bourgeade, A., Le Floch, P. and Raviart, P. A., Approximate Solution of the Generalized Riemann Problem and Applications, in "Proceedings of Saint-Étienne", Springer Lecture Notes in Mathematics 1270, (1986).
- (11) Bourgeade, A., Le Floch, P. and Raviart, P. A., An Asymptotic Expansion for the Solution of the Generalized Riemann Problem, Part 2: Application to the Equations of Gas Dynamics, Ann. Inst. H. Poincaré, Nonlinear Analysis, Vol. 6 (1989), p. 437.
- (12) Colella, P., Majda, A. and Roytburd, V., Theoretical and Numerical Structure for Reacting Shock Waves, SIAM J. Sci. Stat. Comp., Vol. 7 (1986), p. 1059.
- (13) Courant, R. and Friedrichs, K. O., Supersonic Flow and Shock Waves, (1976), Springer-Verlag, New York.
- (14) Falcovitz, J., Alfandary, G. and Ben-Dor, G., Numerical Simulation of the Head-on Reflection of a Regular Reflection, Int. J. Numerical Methods in Fluids, Vol. 17 (1993), p. 1055.
- (15) Falcovitz, J., Alfandary, G. and Hanoch, G., A two-dimensional Conservation Laws Scheme for Compressible Flow with Moving Boundaries, Preprint No. 7, 1994/95, Institute of Mathematics, The Hebrew University, Jerusalem 91904, Israel.
- (16) Falcovitz, J., Alfandary, G. and Hanoch, G., The GRP Scheme for Multi-Fluid Shock Wave Phenomena, presented at the 11th International Mach Reflection Symposium, Victoria, British Columbia, Canada, June 13-17, 1994.
- (17) Falcovitz, J. and Birman, A., A Singularities Tracking Conservation Laws Scheme for Compressible Duct Flows, in "Shock Waves: Proc. of the 18th Int. Symp. on Shock Waves" (Ed. Takayama, K.), (1991), p. 1107, Springer-Verlag.
- (18) Falcovitz, J. and Birman, A., A Singularities Tracking Conservation Laws Scheme for Compressible Duct Flows, J. Comput. Phys., Vol. 115 (1994), p. 431.
- (19) Godunov, S. K., A Finite-Difference Method for the Numerical Computation of Discontinuous Solutions of the Equations of Fluid Dynamics, Mat. Sbornik, Vol. 47 (1959), p. 271.
- (20) Haas, J. F. and Sturtevant, B., Interaction of Weak Shocks with Cylindrical and Spherical Gas Inhomogeneities, J. Fluid Mech., Vol. 181 (1987), p. 41.
- (21) Hillier, R., Computation of Shock Wave Diffraction at a Ninety Degrees Convex Edge, Shock Waves, Vol. 1 (1991), p. 89.
- (22) Igra, O. and Falcovitz, J., Numerical Solution to Rarefaction or Shock Wave/Duct Area-Change Interaction, AIAA, J., Vol. 24 (1986), p. 1390.
- (23) Kalma, A., Computation of Reacting Flows with High Activation Energy, in "Proc. of the Fourth Int. Symp. on Computational Fluid Dynamics, Vol. I", p. 563 (1991), Univ. of California at Davis.
- (24) Landau, C. D., and Lifshitz, E. M., Fluid Mechanics, 2nd Ed., (1987), Pergamon Press, New York.
- (25) Levy, A., On Majda's Model for Dynamic Combustion, Comm. in PDE, Vol. 17 (1992), p. 657.
- (26) Le Floch, P. and Raviart, P. A., An Asymptotic Expansion for the Solution of the Generalized Riemann Problem, Part I: General Theory, Ann. Inst. H. Poincaré, Nonlinear Analysis, Vol. 5 (1988), p. 179.
- (27) Le Floch, P. and Tatsien, Li, A Global Asymptotic Expansion for the Solution to the Generalized Riemann Problem, Asymptotic Analysis, Vol. 3 (1991), p. 321.
- (28) Noh, W. F., CEL: A Time Dependent Two Space-Dimensional, Coupled Eulerian-Lagrangian Code, in "Methods in Computational Physics", Vol. 3 (1964), p. 117, Academic Press, New York.
- (29) Richtmyer, R. D. and Morton, K. W., Difference Methods for Initial Value Problems, (1967), Interscience, New York.
- (30) Saito, T. and Glass, I. I., Application of Random-Choice Method to Problems in Gas Dynamics, Prog. Aerospace Sci., Vol. 21 (1984), p. 201.
- (31) Sod, G. A., A Survey of Several Finite Difference Methods for Systems of Non-Linear Hyperbolic Conservation Laws, J. Comput. Phys., Vol. 27 (1978), p. 1.
- (32) Strang, G., On the Construction and Comparison of Difference Schemes, SIAM J. Num. Anal., Vol. 5 (1968), p. 506.
- (33) van Leer, B., Towards the Ultimate Conservative Difference Scheme V, J. Comput. Phys., Vol. 32 (1979), p. 101.
- (34) Wang, B. Y. and Wu, R. S., Numerical Investigation of Dusty Gas Shock Wave Propagation along a Variable Cross-Section Channel, in "Shock Waves: Proc. of the 18th Int. Symp. on Shock Waves" (Ed. Takayama, K.), (1991), p. 521, Springer-Verlag.



Joseph Falcovitz

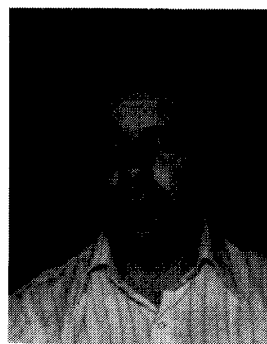
Joseph Falcovitz is currently a Visiting Scientist at the Institute of Mathematics, The Hebrew University of Jerusalem. His major interests are the continued development of high-resolution computational methods for compressible flow, in particular the extensions required to treat phenomena involving moving boundaries and multi-fluid interactions.

He retired in 1990 from the Rafael Ballistics Center where he specialized (since 1971) in the development of computational methods for compressible flow and plasto-dynamics. These methods were applied to the simulation of various terminal ballistics processes such as blast wave and shock wave phenomena, blast-structure interaction, fluid-structure interaction, high-speed jet and projectile penetration, reactive armor and explosively-formed projectiles.

Since 1990 he has held the positions of Associate Professor at the Department of Aerospace Engineering, in the Technion — Israel Institute of Technology, and Visiting Professor at the Shock Wave Research Center of the Institute of Fluid Science in Tohoku University, Sendai, Japan.

Joseph Falcovitz received a PhD degree in Aeronau-

tics and Astronautics from the Massachusetts Institute of Technology in 1970, where he also held the positions of Research Assistant in the Department of Aeronautics and Astronautics and in the Center for Space Research. He was also a Senior Scientist at the Space Systems Academic Group of the Naval Postgraduate School (1985-1987), where he was doing research on continuum and rarefied gasdynamics of plumes in space, and an Adjunct Professor at the Department of Mathematics in the Technion (1987-1989), where he was teaching theoretical hydrodynamics.



Matania Ben-Artzi

Matania Ben-Artzi is a Professor of Mathematics at the Hebrew University of Jerusalem. He is working in various areas of theoretical and numerical mathematical physics, such as scattering and spectral theory, computational fluid dynamics and Navier-Stokes equations.

Matania Ben-Artzi received a PhD degree in mathematics from the Hebrew University of Jerusalem in 1976. He has held various teaching and research positions, including Northwestern University, the University of Minnesota, the University of California at Berkeley, UCLA, the Institute for Advanced Study (Princeton), Paris University and others.